

# On the aerodynamic characteristics of hovering rigid and flexible hawkmoth-like wings

K. B. Lua · K. C. Lai · T. T. Lim · K. S. Yeo

Received: 19 October 2009 / Revised: 20 March 2010 / Accepted: 24 March 2010 / Published online: 9 April 2010  
© Springer-Verlag 2010

**Abstract** Insect wings are subjected to fluid, inertia and gravitational forces during flapping flight. Owing to their limited rigidity, they bent under the influence of these forces. Numerical study by Hamamoto et al. (Adv Robot 21(1–2):1–21, 2007) showed that a flexible wing is able to generate almost as much lift as a rigid wing during flapping. In this paper, we take a closer look at the relationship between wing flexibility (or stiffness) and aerodynamic force generation in flapping hovering flight. The experimental study was conducted in two stages. The first stage consisted of detailed force measurement and flow visualization of a rigid hawkmoth-like wing undergoing hovering hawkmoth flapping motion and simple harmonic flapping motion, with the aim of establishing a benchmark database for the second stage, which involved hawkmoth-like wing of different flexibility performing the same flapping motions. Hawkmoth motion was conducted at  $Re = 7,254$  and reduced frequency of 0.26, while simple harmonic flapping motion at  $Re = 7,800$  and 11,700, and reduced frequency of 0.25. Results show that aerodynamic force generation on the rigid wing is governed primarily by the combined effect of wing acceleration and leading edge vortex generated on the upper surface of the wing, while the remnants of the wake vortices generated from the previous stroke play only a minor role. Our results from the flexible wing study, while generally supportive of the finding by Hamamoto et al. (Adv Robot 21(1–2):1–21, 2007), also reveal the existence of a critical stiffness constant, below which lift coefficient deteriorates significantly.

This finding suggests that although using flexible wing in micro air vehicle application may be beneficial in term of lightweight, too much flexibility can lead to deterioration in flapping performance in terms of aerodynamic force generation. The results further show that wings with stiffness constant above the critical value can deliver mean lift coefficient almost the same as a rigid wing when executing hawkmoth motion, but lower than the rigid wing when performing a simple harmonic motion. In all cases studied ( $7,800 \leq Re \leq 11,700$ ), the Reynolds number does not alter the force generation significantly.

## List of symbols

$A_\phi$	The angle the wing swept over one complete stroke
$B$	Buoyancy (N)
$C$	Chord length (m)
$C_D$	Drag coefficient
$C_L$	Lift coefficient
$C_H$	Horizontal force coefficient
$C_V$	Vertical force coefficient
$EI$	Overall spanwise flexural stiffness ( $N\ m^2$ )
$F$	Force (N)
$F_C$	Chordwise force acting on the wing (N)
$F_D$	Drag force (N)
$\bar{F}_D$	Time-averaged drag force (N)
$F_L$	Lift force (N)
$\bar{F}_L$	Time-averaged lift force (N)
$F_N$	Normal force acting on the wing (N)
$\bar{F}_V$	Time-averaged vertical force (N)
$k$	Wing stiffness (N/m)
$k_c$	Reduced frequency
$k_R$	Wing relative stiffness
$n$	Flapping frequency ( $s^{-1}$ )
$R$	Wing span measured from wing tip to center of rotation (m)

K. B. Lua (✉) · K. C. Lai · T. T. Lim · K. S. Yeo  
Department of Mechanical Engineering,  
National University of Singapore, 9 Engineering Drive 1,  
Block EA, 07-08, Singapore 117576, Singapore  
e-mail: mpelkb@nus.edu.sg

$Re$	Reynolds number
$R_{\text{tip}}$	Wing span measured from wing tip to wing base (m)
$\hat{r}_2$	Dimensionless second moment of wing area
$S$	Surface area of wing ( $\text{m}^2$ )
$T$	Flapping period (s)
$U_{\text{rev}}$	Reference velocity (m/s)
$t$	Time (s)
$t^*$	Nondimensional time = $t/T$
$\Phi$	Sweeping amplitude ( $^\circ$ )
$\alpha$	Angle of attack ( $^\circ$ )
$\dot{\alpha}$	Angular velocities of rotating ( $^\circ/\text{s}$ )
$\beta$	Rotational amplitude ( $^\circ$ )
$\delta$	Average stroke plane angle ( $^\circ$ )
$\varepsilon$	Wing displacement in the stiffness test (m)
$\phi$	Sweeping angle ( $^\circ$ )
$\phi_0$	Sweeping angle offset ( $^\circ$ )
$\dot{\phi}$	Angular velocities of sweeping ( $^\circ/\text{s}$ )
$\nu$	Kinematic viscosity ( $\text{s}/\text{m}^2$ )
$\gamma$	Average wing deflection angle ( $^\circ$ )
$\theta$	Elevation angle ( $^\circ$ )
$\dot{\theta}$	Angular velocities of elevation ( $^\circ/\text{s}$ )
$\rho$	Density ( $\text{kg}/\text{m}^3$ )

### Subscripts

$i$  Initial value

## 1 Introduction

Interest in insect-like micro aerial vehicles (MAV) is on the rise due to the demand for aerial vehicles that are small and able to operate in a confined area (Ellington 1999; Deng et al. 2006a, b). They may carry onboard payloads, such as camera for surveillance missions. It is well known that flight performance of insects far exceeds those of conventional flyers in terms of agility and ability to lift heavy objects relative to their weight and they can even fly upside down.

Insects generate aerodynamic forces by flapping their wings, which consists broadly of sweeping and rotational motions. This mode of locomotion is different from that of a conventional aircraft wing where smooth and steady or quasi-steady flow is assumed. Sane and Dickinson (2001) have shown that traditional quasi-steady estimates, which exclude the unsteady effects of motion and wake, were not robust enough to predict the forces of an insect wing executing unsteady flapping motions.

Leading edge vortices (LEV), among other unsteady mechanisms, play an important role in enhancing lift generation on insect flapping wings. Past flow visualization revealed the dominance of LEV in butterflies (Srygley and Thomas 2002), hawkmoth (Ellington et al. 1996; Van Den Berg and Ellington 1997) and fruitfly (Dickinson and Gotz

1993; Birch and Dickinson 2001). The existence of LEV was also observed in the numerical simulations of Wu and Sun (2004). The LEV remains attached to the wing throughout the flapping stroke. Various hypotheses have been proposed to explain the prolonged attachment of LEV; Ellington et al. (1996) and Van Den Berg and Ellington (1997) attributed it to the draining of energy from the vortex core by spanwise (or axial) flow analogous to the attached vortex on a delta wing, while Birch and Dickinson (2001) credited it to a reduction in the effective angle of attack due to the downwash induced by wing-tip vortices. A more recent numerical and experimental study by Lim et al. (2009) show that spanwise flow per se may not lead to prolonged attachment of LEV, it must be accompanied by vortex stretching. Other aspects of the unsteady aerodynamics of flapping wing have also been extensively studied (see Platzer et al. 2008; Shyy et al. 2008; Young et al. 2008; Mueller 2001).

Since insect wings are largely passive, and actuation is situated at the wing base, wing deflection is caused primarily by inertial and aerodynamic forces generated due to wing movement. Therefore, the amount of wing deflection is governed by these forces and the wing stiffness. Experiments by Combes and Daniel (2003b) using actual hawkmoth wings in air and helium (15% of air density) found that inertial-elastic forces play a major role in wing bending and that aerodynamic forces only have minor contribution. Past studies have found that wing deformation to be a significant feature in aerodynamic force generation of the flexible insect wings performing unsteady flapping motion (see Wootton 1992; Wootton et al. 2000, 2003). Recent PIV measurements by Mountcastle and Daniel (2009) using fresh real hawkmoth wing (more flexible) and desiccated wing (more rigid) reveal that the flexible wing exhibits greater compliance and induced larger vertical velocity, thus implying larger lift generation.

Force measurements have been conducted on rigid insect wing models in the past using various approaches, including robotic flappers (Dickinson et al. 1999; Lehmann 2004; Isaac et al. 2006; Poelma et al. 2006) and winged propeller (Usherwood and Ellington 2001). As far as we are aware, similar measurement on flexible wings has not been attempted before. This can be partly attributed to the technical difficulty of fabricating wings that deform exactly like that of an insect. Thus, most of the studies on the effect of wing flexibility have been conducted numerically. For example, Smith (1996) developed a numerical code that accounts for both the aerodynamic and the inertia forces on flapping flexible wings in the presence of large-scale vortices. They used panel method for the aerodynamics and the finite element method for the wing structure. More recently, Pederzani and Haj-Hariri (2006) have developed a two-dimensional numerical model for flexible bodies in

unsteady viscous flows, and their results on a flexible wing oscillating in a viscous flow showed that flexible wing undergoing small deflection exhibits higher efficiency than a rigid wing. Similarly, when high efficiency is preferred over high lift generation in the situation such as forward flight, study by Young et al. (2009) reveals that wing deformation enhances the aerodynamic efficiency of locust wings by reducing flow separation and directing aerodynamic force vector to the proper direction. In a related study, Hamamoto et al. (2007) apply finite element analysis, based on the arbitrary Lagrangian–Eulerian method, to study aerodynamic force generation on hovering “two-wing” dragonfly (i.e., two wings instead of four are used to simplify their calculation) and found that flexible wing is able to generate almost the same amount of lift force as the rigid wing. In their integrated experimental and computational study, Zheng et al. (2009) recorded the wing and body kinematics of free flight insects, and then use the data in their computational simulation to study the effect of wing flexibility in insect flight. They observed the formation of spiral leading-edge vortices on the wings, and these vortices are linked to a pair of tip vortices during the downstroke, while vortices are shed from the wing into the wake during the upstroke. The computed average lift of 15 mN matched well with the real insect weight of 13.7 mN.

The finding by Hamamoto et al. (2007) is interesting from the viewpoint of micro aerial vehicle application because it means that a lighter and flexible wing can be used without sacrificing too much of the aerodynamic performance. Here, aerodynamic performance is defined as the performance of a flapping wing in generating aerodynamic forces. However, the result also raises two questions: (1) What is the exact relationship between wing stiffness and aerodynamic force generation? (2) To what extent can wing stiffness be reduced before aerodynamic forces are affected significantly? To answer these questions, we subjected hawkmoth-like wings of different stiffness to hawkmoth flapping motion as well as a simple harmonic motion using a 3-D flapping mechanism and measured the corresponding time-accurate aerodynamic forces. The study was conducted in two stages. The first stage involved detailed force measurements of a rigid hawkmoth-like wing undergoing hovering hawkmoth flapping motion and simple harmonic flapping motion. For the hawkmoth motion, measurements were conducted at Reynolds number ( $Re$ ) of 7,254, sweep angle of the wing (over one complete stroke) of 1.94 radians (i.e.,  $110.96^\circ$ ) and reduced frequency of 0.26. And for the simple harmonic flapping motion, the Reynolds numbers were 7,800 and 11,700, and the wing sweep angle and reduced frequency were 2.09 radians (i.e.,  $120^\circ$ ) and 0.25, respectively. The choice of the Reynolds numbers is dictated by the sensitivity of

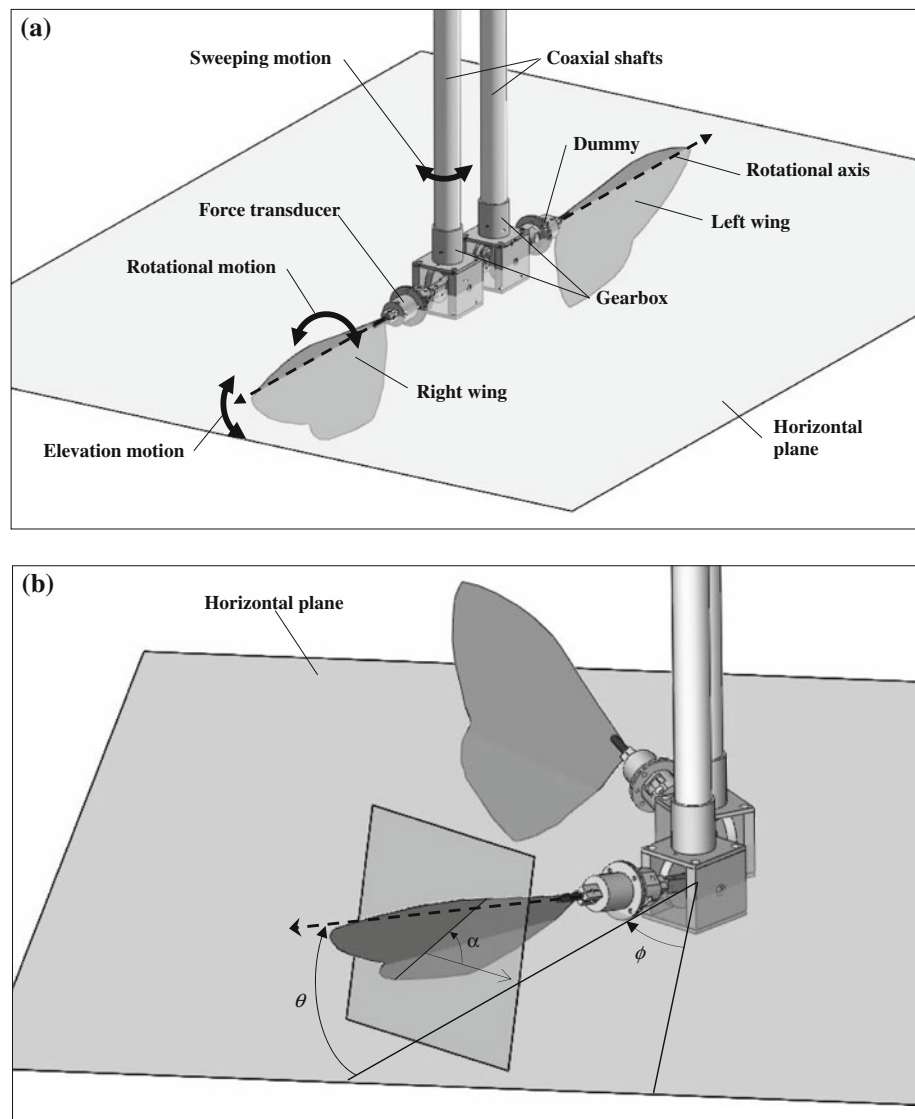
the force sensor. Besides, the results to be presented later show that they are relatively insensitive to the range of Reynolds numbers investigated here. Complimentary flow visualization was also conducted to better understand how the vortex structures generated during the flapping motion affect the transient behavior of the aerodynamic forces. The measurements on the rigid wing serve as benchmark cases for comparison with the corresponding force measurements on flexible wings conducted in the second stage. Unfortunately, the same flow visualization could not be performed on the flexible wings because mounting dye injection tubes on these wings would have significantly altered wing flexibility and affected the flow field. Although dye visualization cannot give quantitative information, such as velocity and vorticity, they give reasonably accurate information about the topological flow structures.

It is worth stressing that although hawkmoth wing model and flapping motion are used in the present study, they are in no way mimicking a real hawkmoth insect because the structural properties of the real wing are significantly more complex to model experimentally. The hawkmoth wing and kinematics are used merely as a means to achieve our aim in a more realistic manner, while at the same time to provide useful data to an existing body of results on hawkmoth motion (Willmott and Ellington 1997a), wing morphology and aerodynamic performance (Willmott and Ellington 1997b).

## 2 Experimental apparatus and procedure

A 3-D flapping wing mechanism is developed for this study and a schematic drawing of it is shown in Fig. 1a. Here, the right hawkmoth wing model was attached to the actuating gearbox via a force transducer, and the left wing was similarly attached via a “dummy” transducer. The gearboxes are driven by three stepper motors through three stainless coaxial transmission shafts. The shafts are 1.5 m long so that when the system is fully assembled, the gearbox, the force transducer and the wings (see Fig. 1a) can be fully immersed at about the middle of a square base tank (1.5 m  $\times$  1.5 m), which is filled with water up to a height of 1.2 m. Figure 1b shows the definition of the three axes of wing motions. Each coaxial shaft controls a particular wing motion, for example, the outer shaft rotates the entire gearbox for sweeping motion ( $\phi$ ), the middle shaft rotates the gears for elevation motion ( $\theta$ ) and the inner shaft rotates the gears for rotational motion ( $\alpha$ ). Specifically,  $\theta$  is the angle between the rotational axis and the horizontal plane,  $\alpha$  is the angle from the horizontal plane to the wing chord and  $\phi$  is the angle between the projection of the rotational axis on the horizontal plane and the line joining the centers of the two coaxial shafts.

**Fig. 1** Schematics of the experimental setup. **a** Shows the definition of the flapping motions, and **b** shows the definition of angle of attack  $\alpha$ , elevation angle  $\theta$  and sweeping angle  $\phi$



All the stepper motors are set at a step-angle of  $0.036^\circ$  and controlled by a Pentium 4 PC through TTL signals from digital I/O card. The motion of the individual stepper motor is computed using a customized program written in LabView. With known motor step sizes and final gear ratios, the program calculates the required TTL pulses to control the motors to achieve the desired motion. To synchronize the wing motion with the force measurement, a triggering signal is sent from the digital I/O card to the trigger input of the data acquisition card when the wings are set in motion.

Fluid dynamic forces acting on the wing are measured by the above-mentioned force transducer attached to the base of the right wing only (see Fig. 1). The force transducer detects forces and moments in two axes by means of strain gages attached to the bending beam section of the transducer. The operation of the force transducer is based on the principle of a double bending beam as illustrated in

Fig. 2. By proper arrangement and wiring of the strain gages mounted on the beam, the force and moment acting on the beam can be measured using four strain gages for each of the axes. Figure 2a shows the measurement of a normal force  $F_N$  acting on the force transducer. This particular force results in bending strains of equal magnitude and opposite sign at the strain gage positions S1 and S2 as indicated in Fig. 2b. Subtraction of the calibrated strain gage signal at S1 from that at S2 gives the normal force signal  $F_N$ . Figure 2c shows the measurement of moment  $M_N$  that results in a constant bending moment along the beam as shown in Fig. 2d. Summation of the S1 and S2 signals gives the signal  $M_N$ . With the same arrangement, attaching strain gages to the other two sides of the bending beam enables measurement of the force ( $F_c$ ) and moment ( $M_c$ ) in the chordwise axis. This arrangement of the strain gages enables simultaneous force and moment measurements with minimal interference from each other. Detail of

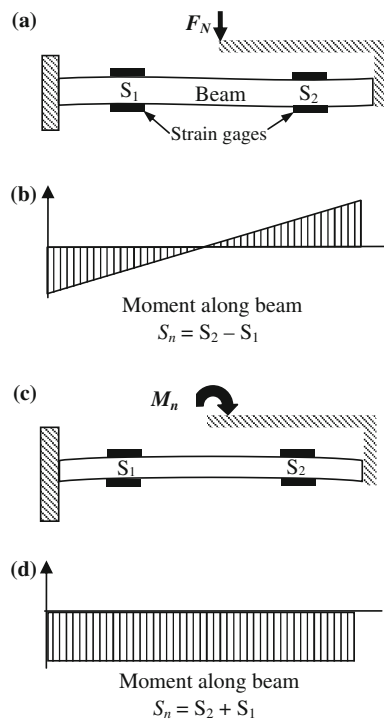


**Fig. 2** Arrangement of strain gages (black boxes) inside the force transducer

how this is carried out in the actual experiment is discussed below.

Each pair of the strain gages has a nominal resistance of 120 Ω each, and they were connected to a Wheatstone bridge in a half bridge configuration, which allowed the strain gage pair to be sensitive only to bending moment on the beam. For ease of reference, the corresponding voltage outputs from the Wheatstone bridges are referred to as  $S_1$ ,  $S_2$ ,  $S_3$  and  $S_4$ . These signals were summed or subtracted using operational amplifiers to obtain the required force and moment signals that are referred to as  $S_N$ ,  $S_C$ ,  $S_{MN}$  and  $S_{MC}$ . The signals were passed through Butterworth low pass filters with a cutoff frequency of 10 Hz, which is more than 66 times higher than the maximum flapping frequency. The outputs were then connected to a data acquisition card that converted the analog voltage signals into digital signals. A program written in VEE Pro (version 6.01, Agilent Technologies) sampled the voltage data at a rate of 100 Hz and converted them into forces and moments using a calibration matrix obtained after the calibration of the force transducer, which is briefly outlined below. The control and data flow block diagram is shown in Fig. 3.

The force transducer was calibrated by applying known weights and measuring the corresponding force and moment signals to create a calibration matrix based on the gradient of each load axis. Verification of the calibration

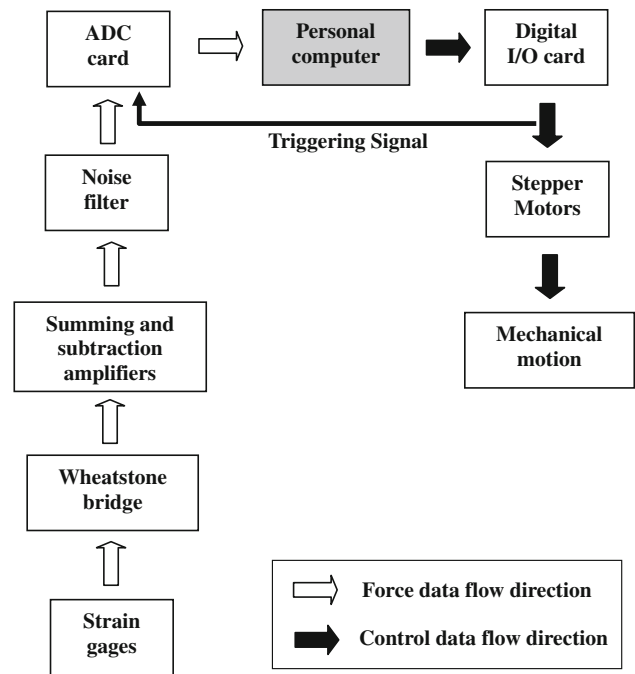


**Fig. 3** Data flow diagram of the apparatus

matrix was carried out by loading known weights at four corners and the center of the wing. Results of the verification showed that the maximum error was less than 5% for the range of forces measured.

The plan form of the hawkmoth wing used in the present experiment is obtained from Liu et al. (1998) (see Fig. 4). The wing models are about five times larger than the real hawkmoth wing as this allows us to match the range of

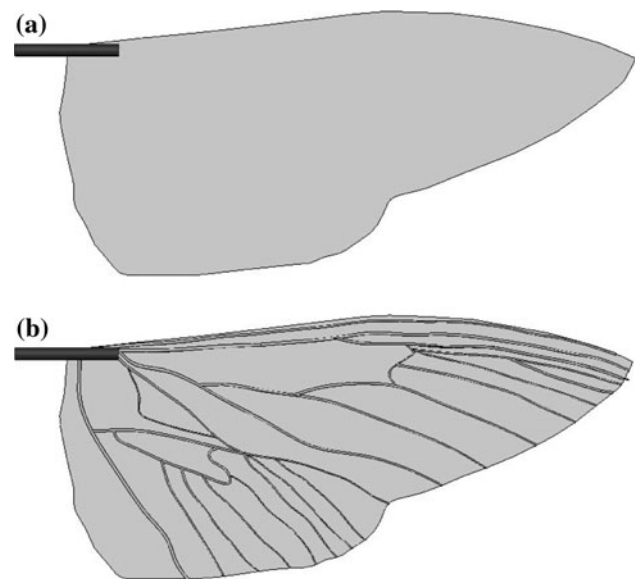


**Fig. 4** Hawkmoth-like wing models used in the present study. **a** Without the veins (i.e., Wing 1 and Wing 2) and **b** with the veins (i.e., Wing 3 to Wing 8)

Reynolds numbers by flapping at lower frequencies. The models were fabricated from materials of different flexibility. To do this, an outline trace of the wing shape was used as a template to cut out wings from the materials. Aluminum sheet of 1.5 mm was used as the reference rigid wing and is referred to as Wing 1. Likewise, 1.5-mm-thick Perspex wing is referred to as Wing 2. Wings 3 to 8 were fabricated using rapid prototyping technology, with wing veins added to the design. The venal geometry is obtained from Wootton et al. (2003). Different flexibility of the wings was achieved by varying the thickness of the wing plane and veins using computer-aided drawing software, Solidworks®. A rapid prototyping (RP) machine (model: Objet Eden 260) was used to fabricate the wings using Fullcure 720 translucent acrylic-based photopolymer. All the RP wings are thin with thicknesses of less than 4% of mean chord length. These materials are used because they provide a range of wing flexibility for this study. Moreover, rapid prototyping machine allowed us to control the wing flexibility in a more measured manner.

The stiffness of each wing was measured using the method similar to that described in Combes and Daniel (2003a) and Mountcastle and Daniel (2009). Figure 5 shows a schematic diagram of the setup, which consists essentially of a modified Instron material characterization machine that is capable of capturing force and displacement data simultaneously. The wing was clamped at its base located near the leading edge, and the load point was at 70% of the wing span. A displacement was applied slowly at the loading point at a rate of 0.2 mm/s, and the resultant point load was measured at a sampling rate of 10 Hz. The

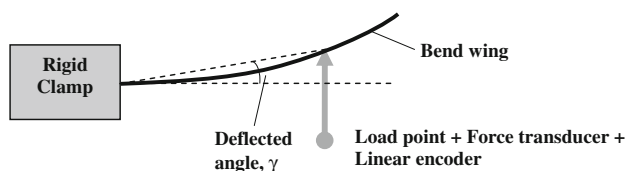


**Fig. 5** Schematic of the experimental setup used to determine wing's stiffness constant

displacement was limited to 12.5 mm that is about 5% of the effective wing span. This restriction is to ensure that wing deflections are within the linear elastic range. The stiffness constant  $k$  (N/m) of each wing was subsequently determined from the gradient of the load versus displacement curve and tabulated as shown in Table 1. Our results show that all the wings exhibit linear behavior except for the “softest” wing (wing 8), which displayed non-linearity with the applied loads. It should be noted that the bending of the wing under applied loads does not coincide with homogeneous beam theory due to non-uniform sectional area of the wing. Also shown in Table 1 are EI and the relative stiffness  $k_R$  of each wing. EI is defined as  $FL^3/3\varepsilon$ , where  $L$  is equal to 70% of the wing span and  $\varepsilon$  is the displacement. It is the overall spanwise flexural stiffness that was presented in Combes and Daniel (2003a) and Mountcastle and Daniel (2009). In order to relate the stiffness of the wing to the aerodynamic force that the wing will experience when flapped, the relative stiffness ( $k_R$ ) is defined as  $kR_{tip}/(1/2\rho U_{ref}^2 S)$ , where  $U_{ref}$  is the reference velocity of the hawkmoth flapping motion, which will be introduced in detail later when  $Re$  is discussed.

Since the flapping motion was oscillatory in nature, the natural frequency of each wing was also measured using an electrodynamic exciter running on the software, VibControl/NT (Vibration Control and Analysis System, m + p international). With the wing secured to an oscillator at the base and the accelerometer mounted at the wing tip, the frequency response of each wing was measured and tabulated in Table 1. The results show that the wing natural frequencies are significantly higher than the maximum flapping frequency of 0.15 Hz used in the present study.

Before the start of each experiment, averaged “reference” voltage values were measured at no load condition for about one second, and all the subsequent measurements were taken relative to their respective no load values. Inertial and gravitational forces were measured by repeating the same experiment in air assuming that the aerodynamic forces in air are relatively negligible. The buoyancy

**Table 1** Wing data

Wing	Material	Stiffness constant, $k$ (N/m)	EI (N m <sup>2</sup> )	Relative stiffness, $k_R$	Natural frequency (Hz)
1	Aluminum	1,694.224	3.027	5,354.872	10.3588
2	Perspex	60.508	0.108	191.2454	10.2105
3	Fullcure 720	45.922	$8.204 \times 10^{-2}$	145.1451	7.7910
4	Fullcure 720	31.265	$5.585 \times 10^{-2}$	98.81905	5.8386
5	Fullcure 720	16.529	$2.953 \times 10^{-2}$	52.2415	6.2077
6	Fullcure 720	7.746	$1.384 \times 10^{-2}$	24.48298	5.6522
7	Fullcure 720	3.950	$7.057 \times 10^{-3}$	12.48329	3.3517
8	Fullcure 720	1.889	$3.375 \times 10^{-3}$	5.970981	2.5504



force  $B$  was obtained by finding the difference in the weight of the wing in air and in water. The weight of the wing was measured by first taking the voltage of  $F_c$  when it was directed normal to the direction of gravity (i.e., reference voltage), and the voltage was taken again when the sensor and wing had rotated through  $90^\circ$  about the angle of attack axis (i.e., when  $F_c$  is parallel to gravity). The difference in the measured readings before and after the rotation is the weight of the wing. The buoyancy forces acting on the wing when immersed in the water were calculated using the following equations

$$F_C^{\text{Buoyancy}} = B(\cos(\theta_i) \sin(\alpha_i) - \cos(\theta) \sin(\alpha)) \quad (1)$$

$$F_N^{\text{Buoyancy}} = B(\cos(\theta) \cos(\alpha) - \cos(\theta_i) \cos(\alpha_i)) \quad (2)$$

where  $F_C^{\text{Buoyancy}}$  and  $F_N^{\text{Buoyancy}}$  are the resolved forces in the chordwise and normal direction. The inertia, gravity and buoyancy data were subtracted from the measured experiment data, and the final results obtained indicate the contribution of aerodynamic forces only.

Note that in all the force measurements reported here, only the right wing was subjected to the flapping motion and the left wing was not activated. Our preliminary study with two wings executing hawkmoth motion did not show noticeable difference in the measured forces compared to only the right wing operating. This observation is in agreement with the finding of Lehmann et al. (2005), which shows that the effects of wing–wing interaction are significant only when the angular separation of wing pairs is less than  $10^\circ$ – $12^\circ$ . Here, it is about  $68^\circ$ .

Each set of the experiments consisted of six flapping cycles and was repeated four times. There was a waiting time of at least 3 min between successive runs. Preliminary test showed that the residue velocity after 3 min had no noticeable effect on the force measurement. Also, a series of tests were conducted with a false wall located at various distances from the flapping wing, and the result shows that the side walls of our setup do not have noticeable effect on the force measurements, and the tank gives a good approximation of an infinite volume.

There are several derived quantities for the wing configuration namely, deflection angle of the wing ( $\gamma$ ) (see Fig. 5), the dimensionless second moment of wing area ( $\hat{r}_2$ ), the reference velocity ( $U_{\text{ref}}$ ) and Reynolds number ( $Re$ ). The derivation of these quantities is described below. Deflected angles of the wings ( $\gamma$ ) during flapping were estimated from the measured normal force acting on the wings based on the assumption that the deflection follows a linear behavior. The time-averaged absolute normal force ( $\bar{F}_N$ ) acting on the wing for a single flapping cycle was used for this purpose, and it is assumed to be acting at 49% wing span position, which is known to be the aerodynamic center (Weis-Fogh 1973). For such calculation, the

stiffness constant  $k$  of the wing at 49% wing span position was interpolated from that at 70%. The estimated displacement was then converted into deflection angle  $\gamma$  using the following equation

$$\gamma = \tan^{-1} \left( \frac{\bar{F}_N}{0.7kR} \right). \quad (3)$$

As for the force coefficients and Reynolds number, they were computed using the second moment of wing area, which is the convention used by Ellington (1984). To determine the second moment of area, a scanned picture of the fabricated wing plan form was first plotted on a spreadsheet program. Next, two lines representing the leading edge and trailing edge, each consisting of 59 equally spaced points, were plotted over the wing outline in the picture, and the co-ordinates of each point were noted. Using the co-ordinates of the 59 points, the picture of the wing was then subdivided into 58 small strips parallel to the chordline, the area was calculated by approximating each strip as a trapezium. The calculated area was then scaled appropriately to find the actual area of the wing.

Since the rotational axis of the wing does not coincide with the wing base but is located at a radial distance of 0.1131 m, this offset radial distance was added to the  $R$  values of the formula used to calculate the actual second moment of wing area around the sweeping axis.

$$\begin{aligned} \hat{r}_2^2 &= \left( \int_0^R cR^2 dR \right) / (SR^2) \\ &= \left( \sum_{x=1}^{58} 0.5h[c_z + c_{z+1}](R_z + \text{Offset distance})^2 \right) / (SR^2) \end{aligned} \quad (4)$$

where  $c_z$  is the chord length of the wing for the particular elemental strip  $z$  located at a spanwise position  $R_z$  and  $h$  is the width of each strip.

Reynolds number is defined as  $Re = \bar{c}U_{\text{ref}}/\nu$ , where  $\nu$  is the kinematic viscosity of water and  $U_{\text{ref}}$  is the reference velocity given by  $U_{\text{ref}} = \bar{\omega}\hat{r}_2R$ . Averaged angular velocity is defined as  $\bar{\omega} = 2A_\phi n$ , where  $A_\phi$  is the angle swept by the wing over one complete stroke. The rigid model (Wing 1) has a span of 0.25 m, mean chord ( $\bar{c}$ ) of 0.07581 m and surface area ( $S$ ) of 0.01963 m<sup>2</sup>. The dimensionless second moment of area ( $\hat{r}_2$ ) of the wing area about the center of rotation is 0.654. The radial distance of the wing tip from the flapping axis ( $R$ ) is 0.3615 m. These values were used to calculate the Reynolds number ( $Re$ ) for all the wings. The temperature of water during the experiment was 22°C, giving the corresponding kinematic viscosity,  $\nu = 9.570 \times 10^{-7}$  m<sup>2</sup>/s and density,  $\rho = 997.86$  kg/m<sup>3</sup>. The reduced frequency based on the mean chord length is defined as  $k_c = \pi n \bar{c} / U_{\text{ref}} = \pi \bar{c} / 2A_\phi \hat{r}_2 R$ .

Two flapping motions were investigated here, namely the hawkmoth hovering motion and a simple harmonic motion. Hawkmoth motion was chosen because detail kinematic is readily available in the literature and it was determined by curve fitting the measurements of the hovering motion of a male hawkmoth obtained by Willmott and Ellington (1997a). The  $Re$  for the real hawkmoth is around 3,000 to 4,000 (based on mean chord length of 1.83 cm, wing length of 4.83 cm,  $\hat{r}_2$  of 0.52 and flapping frequency of 26.1 Hz and the reduced frequency  $k_c$  is reported to be 0.37.

A computer program written in LabVIEW made use of the splined interpolation scheme to fit the curves. Each motor position was determined by its individual starting position, and the subsequent motion (in micro steps) was determined from the curve obtained. To do this, a computer program calculated the corresponding time for each of the motor micro steps. Figure 6a shows the sweeping angle ( $\phi$ ), angle of attack ( $\alpha$ ) and elevation angle ( $\theta$ ) of a hawkmoth flapping motion. For the hawkmoth motion under investigation,  $A_\phi$  is 1.94 radians (i.e., 110.96°), Reynolds number ( $Re$ ) is 7,254, reduced frequency ( $k_c$ ) is 0.26 and the flapping frequency ( $n$ ) is 0.1 Hz. The wing size and flapping frequency were chosen to match the optimal operating range of the equipment.

The simple harmonic flapping motion is defined by the following equations:

$$\text{Sweeping angle: } \phi(t) = \phi_0 + \Phi \cos(2\pi n_\phi t) \quad (5)$$

$$\text{Angle of attack: } \alpha(t) = 90^\circ - \beta \sin(2\pi n_\alpha t) \quad (6)$$

where  $\Phi$  is the amplitude of the sweeping motion and  $\beta$  the amplitude of the rotational motion. Their respective flapping frequencies ( $n_\phi$ , and  $n_\alpha$ ) expressed in Hz are shown in Table 2 together with the corresponding  $Re$ . In the present study,  $\Phi = 60^\circ$ ,  $\phi_0 = 0^\circ$ ,  $\beta = 45^\circ$  and  $k_c = 0.24$ . The relationship between  $\phi$  and  $\alpha$  for the simple harmonic motion is shown graphically in Fig. 6b.

For all the cases investigated here, it is obvious from Eq. 6 that a higher value of  $\beta$  leads to a higher rate of pitching of the wing, and therefore a rapid change in the effective angle of attack.

Lift ( $F_L$ ) and drag ( $F_D$ ) were extracted from the forces normal ( $F_N$ ) and parallel ( $F_C$ ) to the wing using the following equations (see also Fig. 7).

$$F_L = F'_L \cos \theta \quad (7)$$

$$F_L = \cos \theta (F'_L) = \cos \theta (F_N \cos \alpha - F_C \sin \alpha). \quad (8)$$

$$F_D = F_N \sin \alpha + F_C \cos \alpha \text{ (Downstroke)} \quad (9)$$

$$F_D = -F_N \sin \alpha - F_C \cos \alpha \text{ (Upstroke)}. \quad (10)$$

The direction and location of the forces are shown in Fig. 7, bearing in mind that  $F_N$  is normal to the wing surface, and  $F_C$  is coincident with the wing plane and

**Fig. 6** Trajectories of (a) hawkmoth motion, and (b) simple harmonic motion

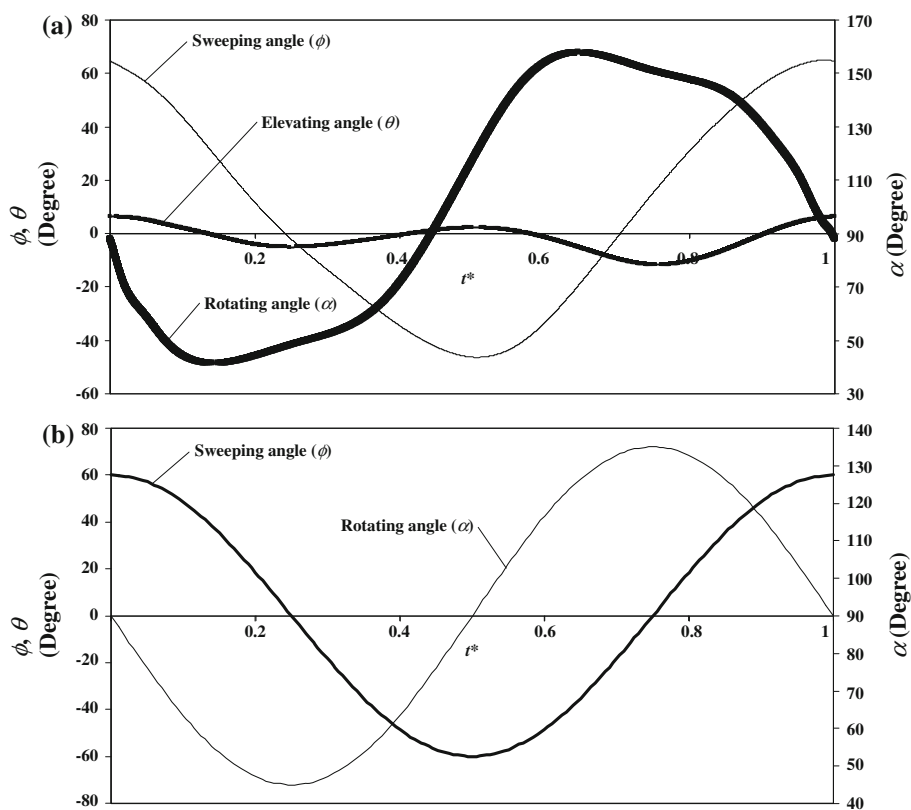




**Table 2** Experimental parameters for simple harmonic motion

Annotation	$Re$	$n_\phi, n_\alpha$ (Hz)
Low	7,800	0.10
High	11,700	0.15

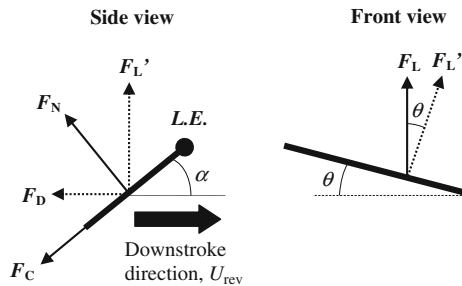


**Fig. 7** Definition of force vectors on the wing.  $F_N$  and  $F_C$  are forces measured by the force sensor. L.E. = Leading edge of the wing

directed in the chordwise direction from the leading to the trailing edge normal to the rotational axis.

Lift and drag coefficients are given by

$$C_L = \frac{2F_L}{\rho U_{ref}^2 S} \tag{11}$$

$$C_D = \frac{2F_D}{\rho U_{ref}^2 S} \tag{12}$$

The motion is based on the local coordinate system. For purpose of comparison, an average stroke plane angle  $\delta$  can be defined as (following Willmott and Ellington 1997a)

$$\tan \delta = \bar{F}_D / \bar{F}_L \tag{13}$$

The calculated angle was used to resolve the forces in the local coordinates to the global coordinates of vertical and horizontal forces as shown in Fig. 8.

$$C_V = C_D \sin(\delta) + C_L \cos(\delta) \tag{14}$$

$$C_H = C_D \cos(\delta) - C_L \sin(\delta) \tag{15}$$

Flow visualization was conducted on the rigid wing by releasing dye through plastic tubes at five strategic

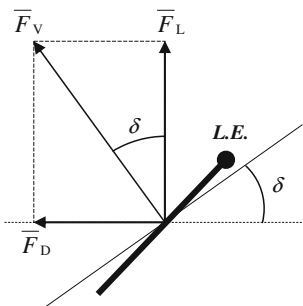


**Fig. 8** Definition of stroke plane inclination angle ( $\delta$ ). L.E. = Leading edge of the wing

locations along the edges of the wing (see Fig. 9). The choice of the dye injection positions is dictated by the locations where the salient features of the flow are expected to be produced. These include the leading edge vortex (LEV), trailing edge vortex (TEV), root vortex (RV) and tip vortex (TV). To minimize flow interference, highly flexible dye injection tubes of the same thickness as the wing were attached to the outer edge of the wing by following its profile. While this can be accomplished with the rigid wing without affecting the vortex dynamics significantly, the same cannot be done with the flexible wings, as the tube would undoubtedly affect the rigidity of the wing. Nevertheless, we believe that the results of the rigid wing can still provide useful clue about the vortex structures on the flexible wings. A Nikon D90 digital camera equipped with 18–105 mm f/3.5–5.6G ED VR Zoom Lens was used to capture the flow images in a high definition video format (1,280 × 720 pixels at 24 fps). Two viewing angles were selected to capture these flow images; the first one involved locating the camera at the side of the flapping mechanism, and the second one with the camera at the front, in two separate runs. Although this is tedious and time-consuming, it is unavoidable since only one camera is available for this investigation. The information from these two viewing angles was used to reconstruct the flow pattern. Flow visualization was conducted on one of the wings only, as the other wing executing the same motion is expected to produce similar flow structures. It is also worth noting that the dye visualization and force measurement were not conducted simultaneously, because the presence of dye injection tubes would contaminate the force measurements. As the force sensor is a fragile instrument, it is replaced by “dummy” with the same shape and dimensions during flow visualization. Unfortunately, we were also unable to conduct DPIV measurements during the flapping motion, due

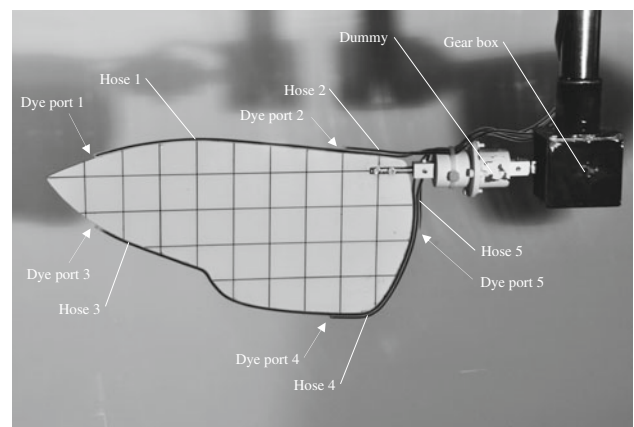


**Fig. 9** Flow visualization experiment showing the locations of dye ports

partly to technical constraints of the experimental setup and partly to the 3-D nature of the flapping motion.

### 3 Results and discussion

#### 3.1 Hawkmoth motion

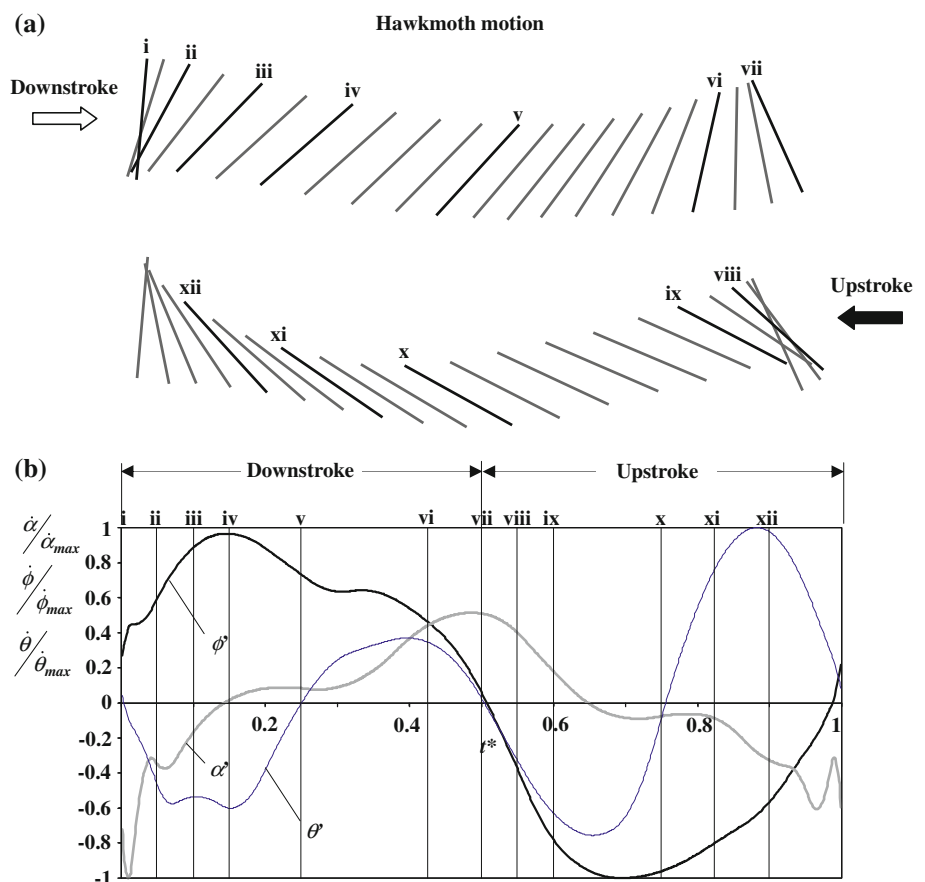
##### 3.1.1 Rigid wing

Figure 10 schematically shows the motion of a rigid wing performing one complete cycle of hawkmoth flapping motion. The associated position and the angle of attack of the wing chord (at the location of second moment of wing area) over forty equal time intervals are shown in Fig. 10a, and the corresponding angular velocities of sweeping ( $\dot{\phi}$ ), elevating ( $\dot{\theta}$ ) and rotating ( $\dot{\alpha}$ ) are shown in Fig. 10b. To better understand how lift and drag are generated, it is useful to note some of the salient features of the hawkmoth flapping motion. Generally, the wing travels with a larger angle of attack during the downstroke and a larger variation in the elevation angle during the upstroke (see Fig. 10a). Also, a large sweeping acceleration (see  $\dot{\phi}$  curve in Fig. 10b) that occurs at the beginning of downstroke has an important implication on the force generation during this

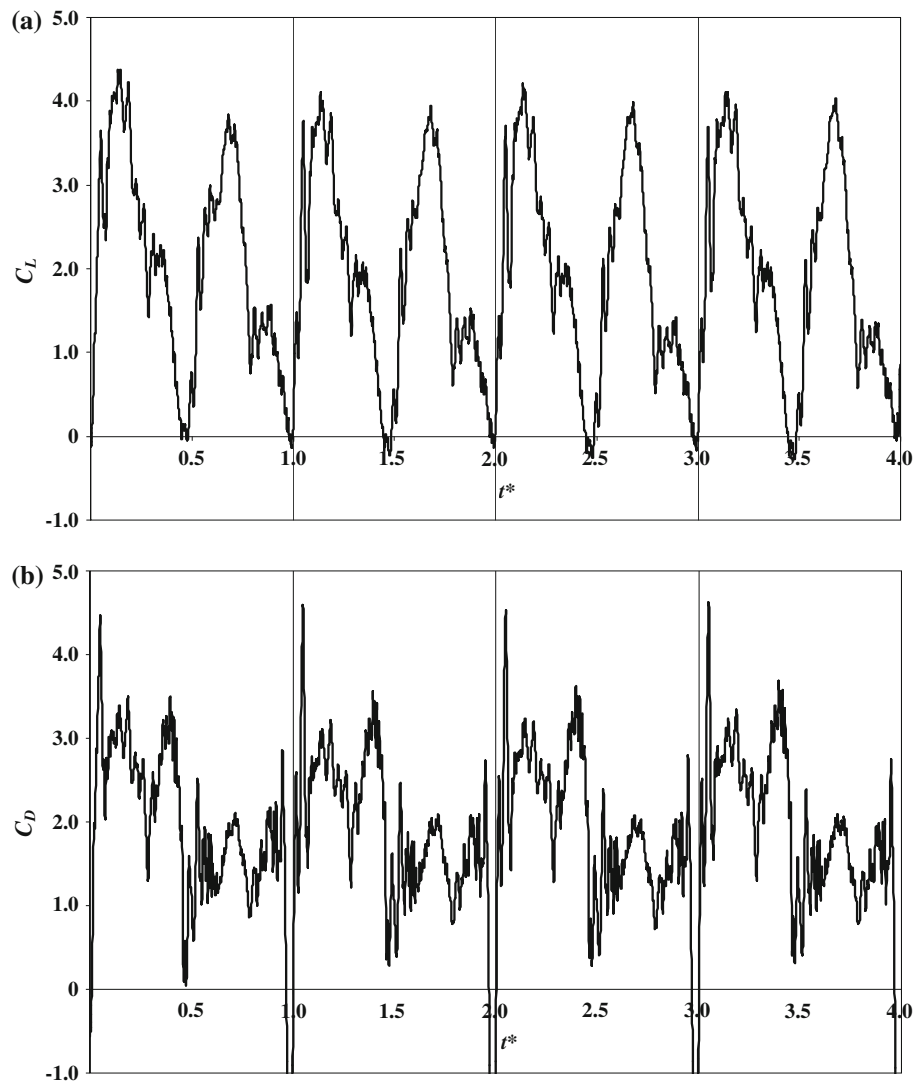
period. The maximum sweeping velocity occurs at  $t^* \approx 0.150$  during the downstroke and at  $t^* \approx 0.700$  during the upstroke, which mean that the wing starts to slow down even before it reaches the middle of each stroke. Around the middle of each stroke, the wing pitches up rapidly after reaching a minimum  $\alpha$  value, and this pitching up motion will have a positive effect on lift generation.

In general, the transitory state occurs during the first four cycles of flapping. Figure 11 shows the time history of the lift and drag coefficients for the first four cycles for the rigid wing. These force coefficients reach periodic state quickly after the second cycle of flapping. Figure 12a, b are the enlarged views of the fourth cycle, showing the details of the force distributions after the initial transient. Since the downstroke motion is quite distinct from the upstroke motion as Fig. 10 clearly shows, it is not a surprise to see the wing generating asymmetric force distributions. Based on these results and together with Eq. 13, it can be shown that the average stroke plane angle  $\delta$  is approximately  $15.3^\circ$  for the hawkmoth flapping motion. This angle is consistent with that obtained by Willmott and Ellington (1997a). Using the average stroke plane angle, the lift and drag in the local stroke plane can be readily converted into vertical and horizontal forces in the global coordinate

**Fig. 10** Hawkmoth flapping motion. **a** Schematic drawing of wing positions and instantaneous angles of attack,  $\alpha$ . **b** Instantaneous sweeping ( $\dot{\phi}$ ), elevating ( $\dot{\theta}$ ) and rotating ( $\dot{\alpha}$ ) velocities for one flapping cycle



**Fig. 11** Time history of lift and drag coefficients for the first four cycles of flapping of Wing 1 (i.e., rigid wing) executing a hawkmoth flapping motion. **a** Lift coefficient ( $C_L$ ). **b** Drag coefficient ( $C_D$ )

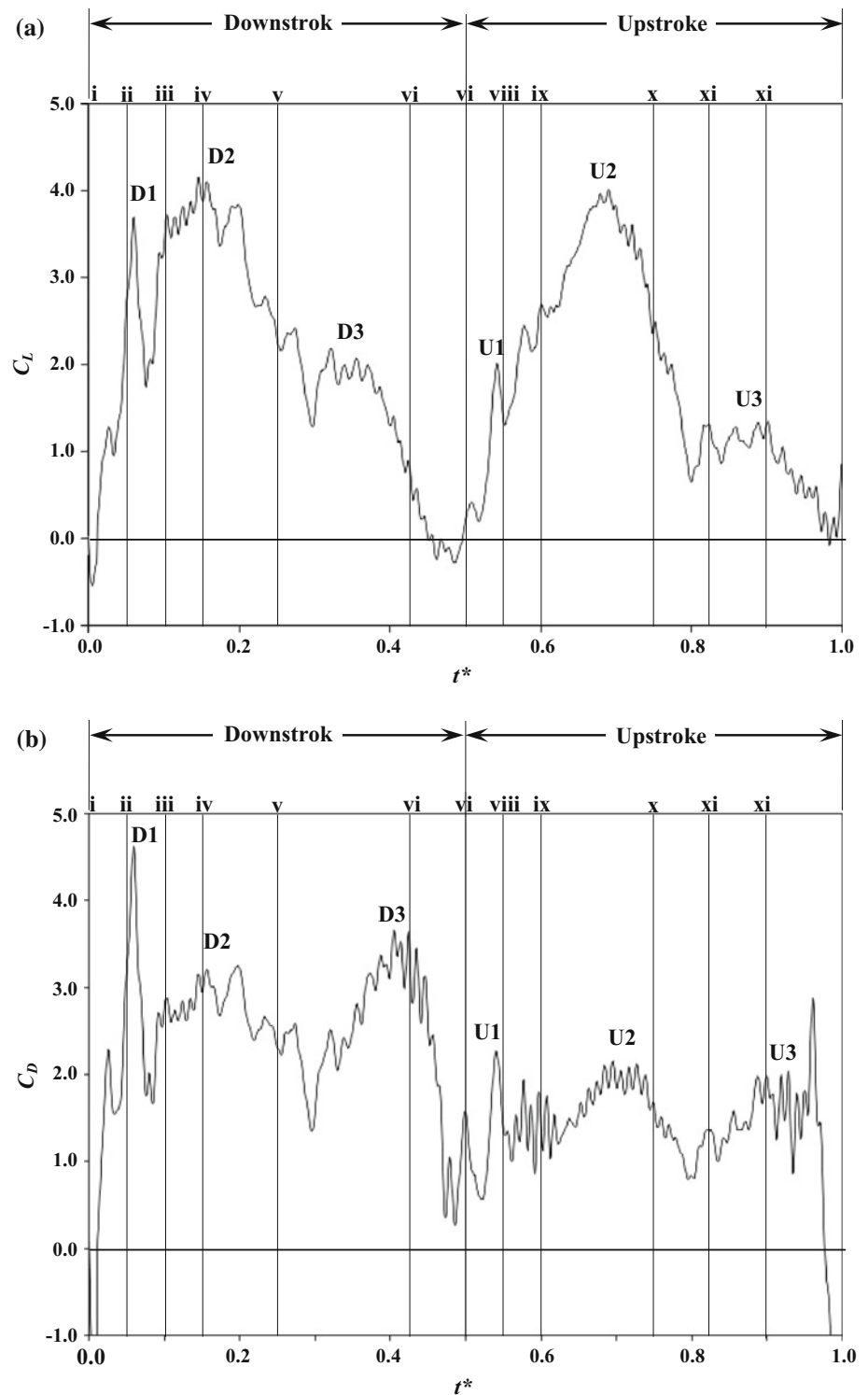


system using Eqs. 14 and 15. When normalized by the square of average velocity, these forces translate into a mean vertical force coefficient ( $C_V$ ) of 2.59 and horizontal force coefficient ( $C_H$ ) of 1.78 during the downstroke, and 1.37 and  $-1.78$ , respectively, during the upstroke. This implies that about 65% of the total vertical force is derived from the downstroke motion. When these forces are averaged over one complete flapping cycle, the mean  $C_V$  and  $C_H$  values are 1.98 and 0, respectively. Willmott and Ellington (1997b), despite using an indirect mean to determine  $C_V$  (see their Fig. 5) for a real hawkmoth performing hovering motion, obtained a  $C_V$  value of 1.84, which is reasonably close to the present experiment of 1.98; the difference is only 7%.

To make sense of the  $C_D$  and  $C_L$  distribution in Fig. 12, we examine closely the video recording of the flow structures during flapping. Figure 13 shows two snapshots of the flow patterns extracted from the video recording. Since it is difficult to convey the dynamics of the flow field through

still pictures, our interpretation of vortices generation and development during flapping, based on the captured video images, are presented in Fig. 14 in both 2-D sectional view and 3-D perspective view. There are a couple of points to note about Fig. 14 before we discuss the results. As highlighted earlier, dye visualization can only give topological structure of the flow and not quantitative information, such as velocity and vorticity. In addition, although Fig. 14i is referred to as the start of the current downstroke, it also coincides with the end of the previous upstroke. Therefore, the vortex (U\_LEV) depicted in the figure is the remnant of the vortex loop shed toward the end of the previous upstroke. Likewise, Fig. 14vii is both the end of the present downstroke and the beginning of the next upstroke. Also, vortices of interest are identified by specific labels, that is,  $D$  denotes the downstroke and  $U$  the upstroke. Furthermore, leading edge vortex, trailing edge vortex, tip vortex and root vortex are identified by LEV, TEV, TV and RV, respectively. For ease of comparison with the measured

**Fig. 12** Time histories of lift and drag coefficients of Wing 1 (i.e., rigid wing) executing a hawkmoth flapping motion. ( $Re = 7,254$ )



forces, each frame in Fig. 14 is identified with the same label as the corresponding forces in Fig. 12. For example, the vortex structure depicted in part (ii) of Fig. 14 corresponds to the drag and lift coefficients indicated by the vertical line with the same label (ii) in Fig. 12. Although the vortex sheet is 3-D in nature, it is represented by only a

line in the 3D perspective view for simplicity, because the inclusion of a complete vortex sheet may complicate the drawing.

Figure 12 clearly shows that the early phase of the downstroke is dominated by a steep increase in  $C_L$  and  $C_D$  up to the first peak identified as D1. The sharp rise in the

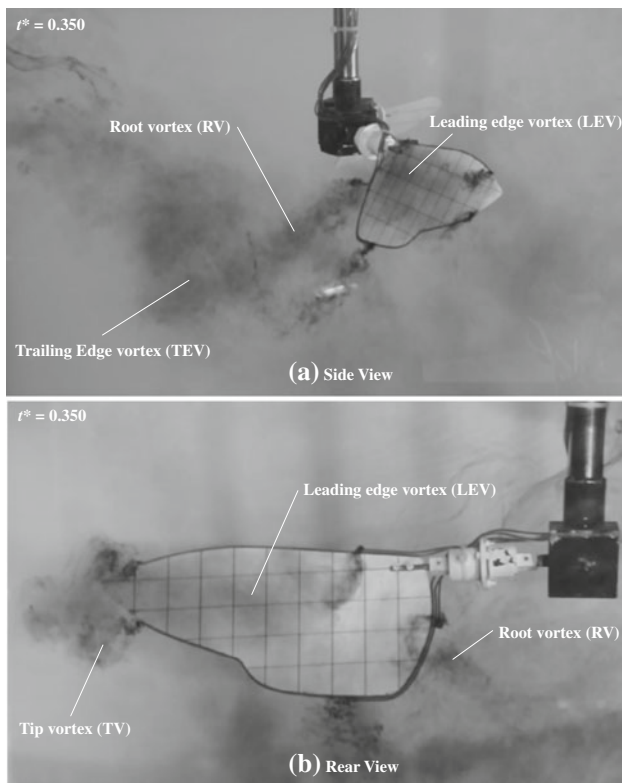


**Fig. 13** Snapshots of flow structure generated during downstroke of a hawkmoth motion. **a** Side view, and **b** front view. Pictures are extracted from video recording

force coefficients can be traced mostly to the effect of added mass as a result of the wing acceleration, and partly to the generation of a vortex loop on the wing surface as can be seen in Fig. 14ii. After reaching the first peak, the lift drops considerably before regaining its magnitude to reach the second and higher peak (D2) at  $t^* = 0.150$ . The initial drop in the lift can be attributed to a reduction in the wing acceleration, and the increase that follows can be traced to the suction lift of the growing LEV attached to the upper surface of the wing as depicted in Fig. 14ii–iv. The wing, after reaching the peak velocity (indicated by (iv) in Fig. 10b), started to decelerate. The effect of reducing the sweeping velocity is reflected in the reduction in lift, which continued until the wing starts to pitch-up rapidly around the middle of the stroke as can be deduced from Fig. 10a. The high pitching rate causes a momentary increase in the lift to reach the third peak (D3) at  $t^* = 0.250$  (see Fig. 10b). As the sweeping velocity continues to decrease and the angle of attack continues to increase until the end of the downstroke, the lift is eventually reduced to near zero value. By this time, the LEV has already shed from the wing leading edge as can be seen in Fig. 14vii, and the wing is about to start a new upstroke. During the upstroke, both the lift and the drag coefficients display a similar

pattern, although at reduced magnitudes as are indicated by  $U_1$ ,  $U_2$  and  $U_3$  in the Fig. 12.

Broadly speaking, the development of flow structure during each stroke of flapping motion can be categorized into three stages, namely the “initial stage”, the “vortex formation stage” and the “finishing stage”. The initial stage of the downstroke extends from  $t^* = 0.000$  to 0.100 and is characterized by the wing accelerating and sweeping into the vortices generated during the previous upstroke. The remnant of the vortex loop from the previous upstroke can be seen in Fig. 14i, and by the time, the wing is about to start the downstroke, most of it has already shed into the wake, although a small portion of  $U_{LEV}$  linking to the  $U_{RV}$  is still attached to the wing. The  $U_{LEV}$  and  $U_{TV}$  appear to be weak and diffused relative to the  $U_{RV}$  as far as we can gather from the dynamics of the dye streak during the replay of the video recording. These vortices, which originated from the vortex sheet emanating from the edges of the wing, are clearly shown in the authors’ interpretation in both the 2-D and the 3-D schematic drawings. As highlighted earlier, the vortex sheet is indicated by a representative line on the cross-sectional plane that is coincidental with the second moment of wing area ( $\hat{r}_2R$ ) for simplicity. As the wing accelerates (see Fig. 14ii), the flow around the edges of the wing begin to separate and roll up to form a vortex loop with the approximate shape of the wing profile. The formation of the loop-shape vortex is a result of the wing not attaching to “insect body”. If the body is present, a horseshoe shape vortex would be formed instead, as observed in Aono and Liu (2008) and Aono et al. (2009). The formation of this vortex loop is partly responsible for the increase in the lift during this early stage of the flapping as was noted earlier. In the 2-D sketches, the portion of the vortex loop at the leading edge is identified as  $D_{LEV}$  and the portion at the trailing edge as  $D_{TEV}$ . The wing motion causes the  $U_{LEV}$  to move further down and  $U_{RV}$  to bend down. By the end of the initial stage (at  $t^* = 0.100$ , see Fig. 14iii), the vortex loop has gained sufficient strength that the portion at the trailing edge is about to shed away.

As the wing enters the second “vortex formation” stage (at  $t^* = 0.150$ , see Fig. 14iv), the portion of the vortex loop at the trailing edge and root edge begins to shed away, to become  $D_{TEV}$  and  $D_{RV}$ , respectively. Near the trailing edge of the wing, the shed  $U_{LEV}$  starts to merge with  $D_{TEV}$ . Since the vortex sheet joining the  $D_{LEV}$  and  $U_{LEV}$  is very thin and diffused, it is omitted in both the 2-D and the 3-D sketches for simplicity. While the  $D_{TEV}$  is shedding away from the wing, our video recording shows that axial flow starts to develop in the  $D_{LEV}$ . As the wing reaches the middle of the downstroke  $t^* = 0.250$ , the flow structure has evolved to the geometry as shown in Fig. 14v. The flow that has separated from the



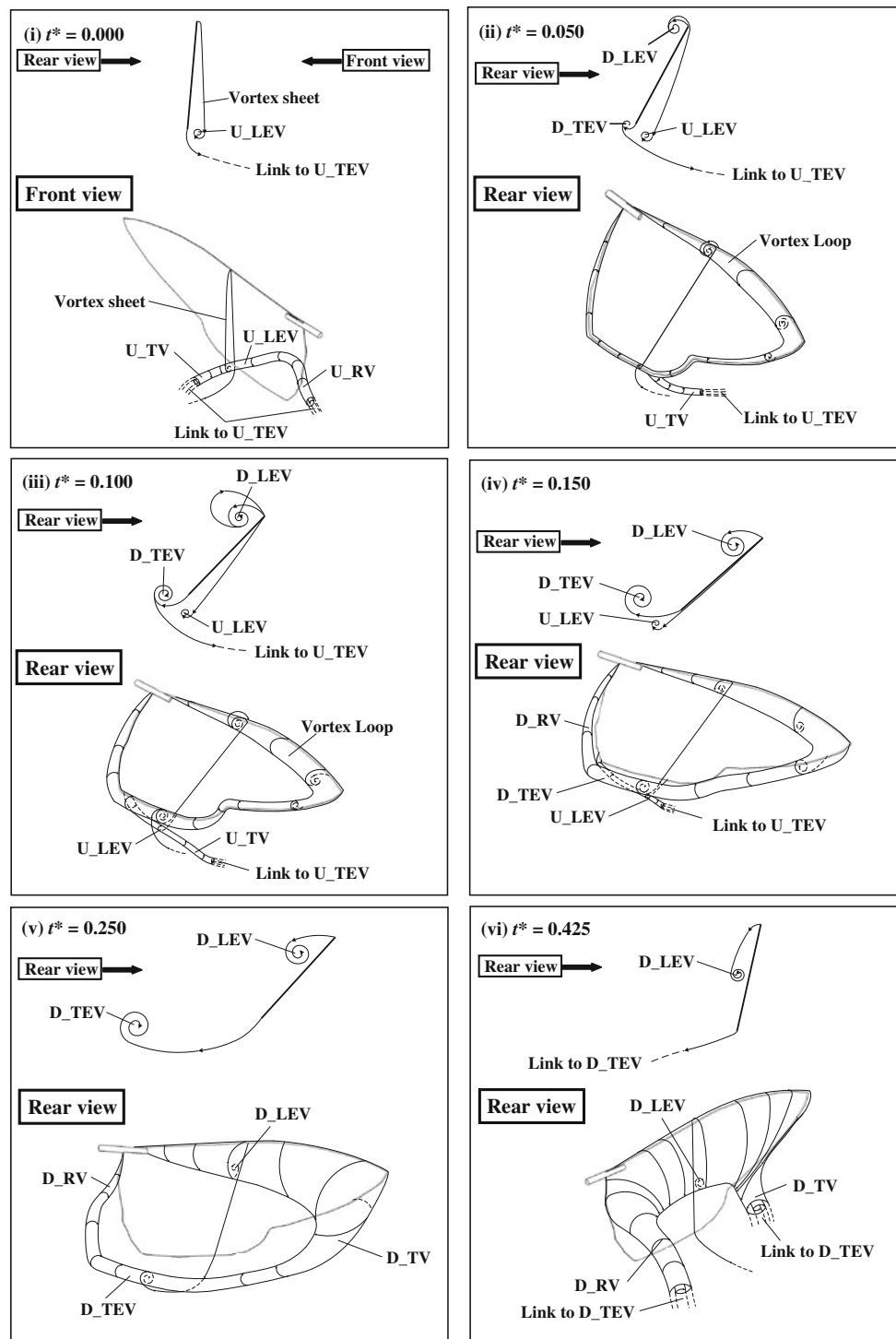


**Fig. 14** Sketches showing the authors' interpretation of the flow development when a rigid wing is executing a hawkmoth motion. Each frame is selected to coincide with the salient features of the force measurements in Fig. 12

proximity of the wing tip rolls up to form D\_TV linking D\_LEV to D\_TEV. The vortex loop becomes distorted as the D\_RV and D\_TV trace the paths of the wing root and tip. Strong axial flow was observed in the D\_LEV from the root toward the tip. The axial flow is expected to carry

away the vorticity shed from the leading edge. The existence of axial flow was also observed by Zheng et al. (2009) when simulating real hawkmoth hovering flight numerically. They noted that the axial flow caused the leading edge vortex to become spiral, and the tip vortex

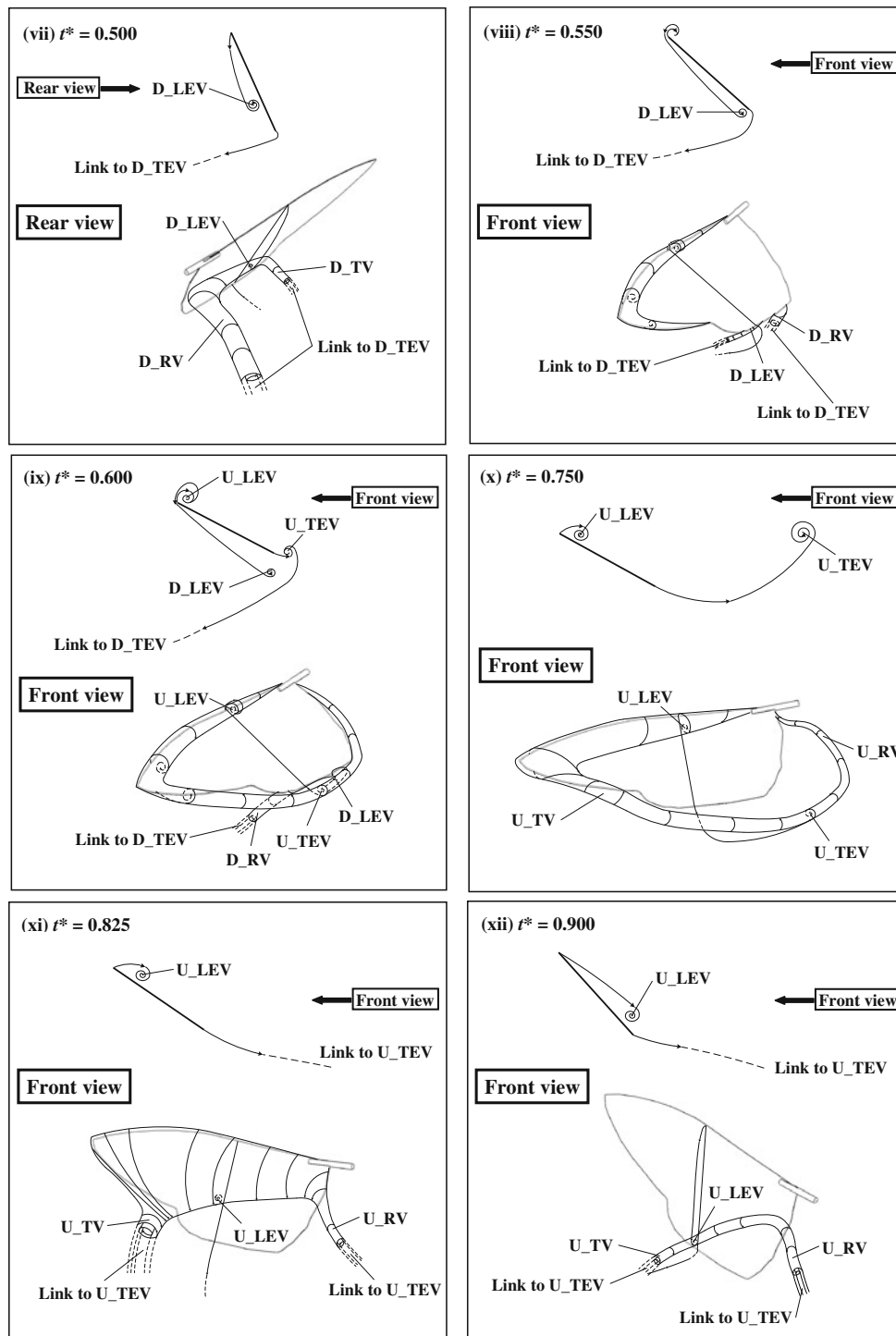
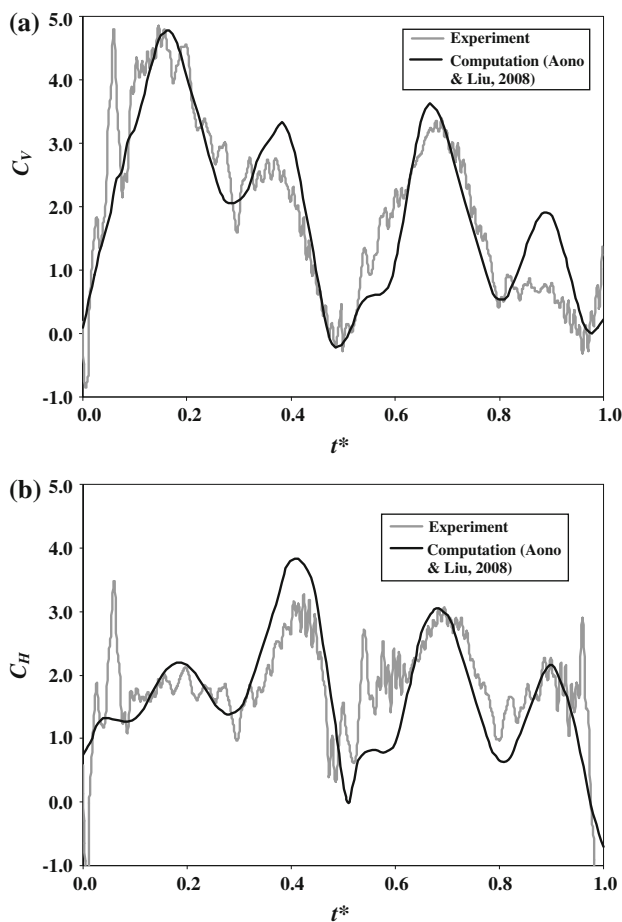


Fig. 14 continued

that linked to the leading edge to extend downstream into the flow.

The third “finishing stage” starts near the end of the downstroke when the wing started to slow down, and at the same time, elevating up and pitching (rotating up). At

$t^* = 0.425$  (see Fig. 14vi), as the wing is sweeping with a low velocity ( $\dot{\phi}$ ) and pitching to high angle of attack, the D\_LEV is observed to weaken rapidly and start to shed from the leading edge. When the downstroke ends at  $t^* = 0.500$  (see Fig. 14vii), the D\_LEV has already



**Fig. 15** Comparison between the forces generated on a rigid wing executing hawkmoth motion and the computation results of Aono and Liu (2008). **a** Vertical force coefficient ( $C_V$ ). **b** Horizontal force coefficient ( $C_H$ )

convected to about two-third the wing chord, and the ensuing viscous diffusion causes it weakened.

In the upstroke, the duration of the three stages of flow development is different due to the obvious difference in wing motion. During the “initial stage” when the wing starts its upstroke motion, flow separating from the leading edge and also from portion of the trailing edge rolls up to form a hook-shape vortex (see Fig. 14viii). This behavior can be attributed to rapid pitching down action (rotating down) by the wing at the beginning of upstroke, causing the trailing edge to move backward (i.e., opposite to the leading edge direction, see Fig. 14vii–viii). As the sweeping velocity increases and the rotational velocity decreases, the flow separation propagates along the rest of the wing profile to form a complete vortex loop. As part of the vortex loop at the trailing edge is shed soon after it is formed, the flow development enters the second “vortex formation” stage (see Fig. 14ix). Although a distorted vortex loop similar to that generated during the downstroke is observed, it appears to be weaker; probably due to a

lower  $\alpha$  (see Fig. 14x). The third “finishing stage” of the upstroke starts early at around  $t^* = 0.825$  (see Fig. 14xi) when the U\_LEV is shed quickly from the leading edge. The rapid shedding of U\_LEV may be due to the fast elevating up motion of the wing, resulting in low effective angle of attack (see Fig. 14xi–xii). The U\_LEV shed quickly from the leading edge toward the trailing edge along the wing upper surface (see Fig. 14xii) and by the time the wing stops at the end of the upstroke, most part of the vortex loop is shed into the flow (see again Fig. 14i).

Comparing the transient force patterns and the corresponding flow structure has given us useful clue to the sources of the peak forces. First, since the LEV generated in previous stroke has already separated from and left the wing, it is reasonable to suggest that the first peak in the force distribution (i.e., D1 or U1) during the downstroke or upstroke is contributed mostly by the wing acceleration and the vortex suction effect of a “young” LEV and not from the induced velocity of the residue LEV as reported in the 2-D experiment of Lua et al. (2008) and 3-D experiment of Dickinson et al. (1999). In the two latter cases, the residue LEV remained attached on the wing surface when the wing reversed its direction and accelerated to start a new stroke.

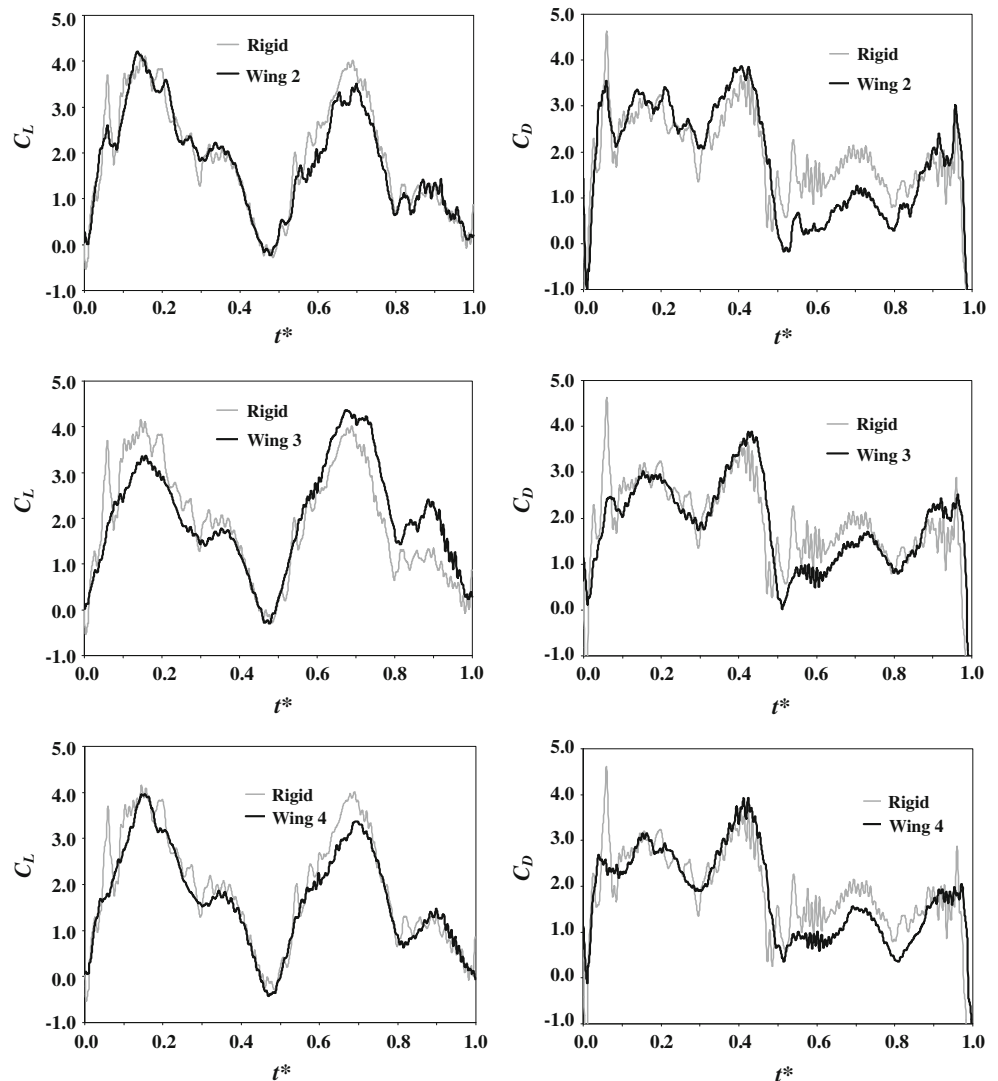
The second peak (D2 or U2), which coincides with the peak in the sweeping velocity, is caused by the increasing wing velocity and the growing LEV. The third peak (D3 or U3), which appears after the wing has slowed down, is due to the wing pitching up (rotating up) motion generating a strong vorticity. Past study by Sun and Tang (2002) shows that strong vorticity shed from the leading edge of the wing during pitching up motion can cause substantial increase in the lift.

Aono and Liu (2008) have recently conducted numerical simulation of a similar flapping motion, and their results (see Fig. 15) show reasonably good agreement with our experiments in terms of the  $C_V$  and  $C_H$  distributions, although details of these distributions are slightly different.

### 3.1.2 Flexible wing

To assess the effect of wing flexibility on the aerodynamic force generation, the same hawkmoth motion was applied to all the flexible wings (Wing 2 to Wing 8), and the results are presented in Fig. 16 together with the benchmark rigid wing case for the purpose of comparison. Figure 16 clearly shows that increasing wing flexibility has a damping effect, which causes a drastic reduction in the peak lift and drag coefficients during the early phase of the downstroke. After the initial attenuation, there are noticeable changes to the lift and drag distributions for Wing 2 to Wing 6. Generally, flexible wings tend to skew the force coefficients curves to the right of the plot, which could be caused by retardation

**Fig. 16** Comparison of the lift and drag coefficients of flexible Wing 2 to Wing 8 with a rigid wing (Wing 1) executing hawkmoth motion. *Left column:* lift coefficient ( $C_L$ ). *Right column:* drag coefficient ( $C_D$ )



in the wing motion during the start of upstroke and downstroke, and this continued to the end of each stroke. Observation during the experiment showed that even after the motion at the base of the wing had come to a stop, the rest of the wing was still moving through the fluid to recover its original shape. Apart from that, the timing and the peak values in lift and drag distributions are not significantly affected by the wing flexibility. This suggests that the overall vortex generation and shedding process of these wings are not significantly different from that of the rigid wing.

On the other hand, Wings 7 and 8 show a substantial reduction in both the lift and the drag. Observation during flapping showed that Wing 8 twisted drastically since it has the lowest stiffness constant. Since the supporting axis is close to the leading edge, the twisting resulted in a reduction in the geometric angle of attack, which may be

partly responsible for a drastic decrease in the force coefficients. Moreover, the bending of the wing in the spanwise direction also causes a reduction in the effective area facing the oncoming flow. In these two cases, not only are the lift and the drag reduced, their distributions have been altered drastically. It is undoubtedly that excessive wing deformation must have affected the vortices and force generation, but as to how they affect the flow fields remains unclear, as we were unable to carry out flow visualization studies for the reason cited earlier. This issue needs further investigation.

To make quantitative comparison with the rigid wing results, the measured forces of the flexible wings are first converted into average  $C_D$  and  $C_L$  values over one cycle and normalized by the corresponding average  $C_D$  and  $C_L$  of the rigid wing (i.e., Wing 1). The results are plotted in Fig. 17 against both the relative stiffness and the stiffness constant.

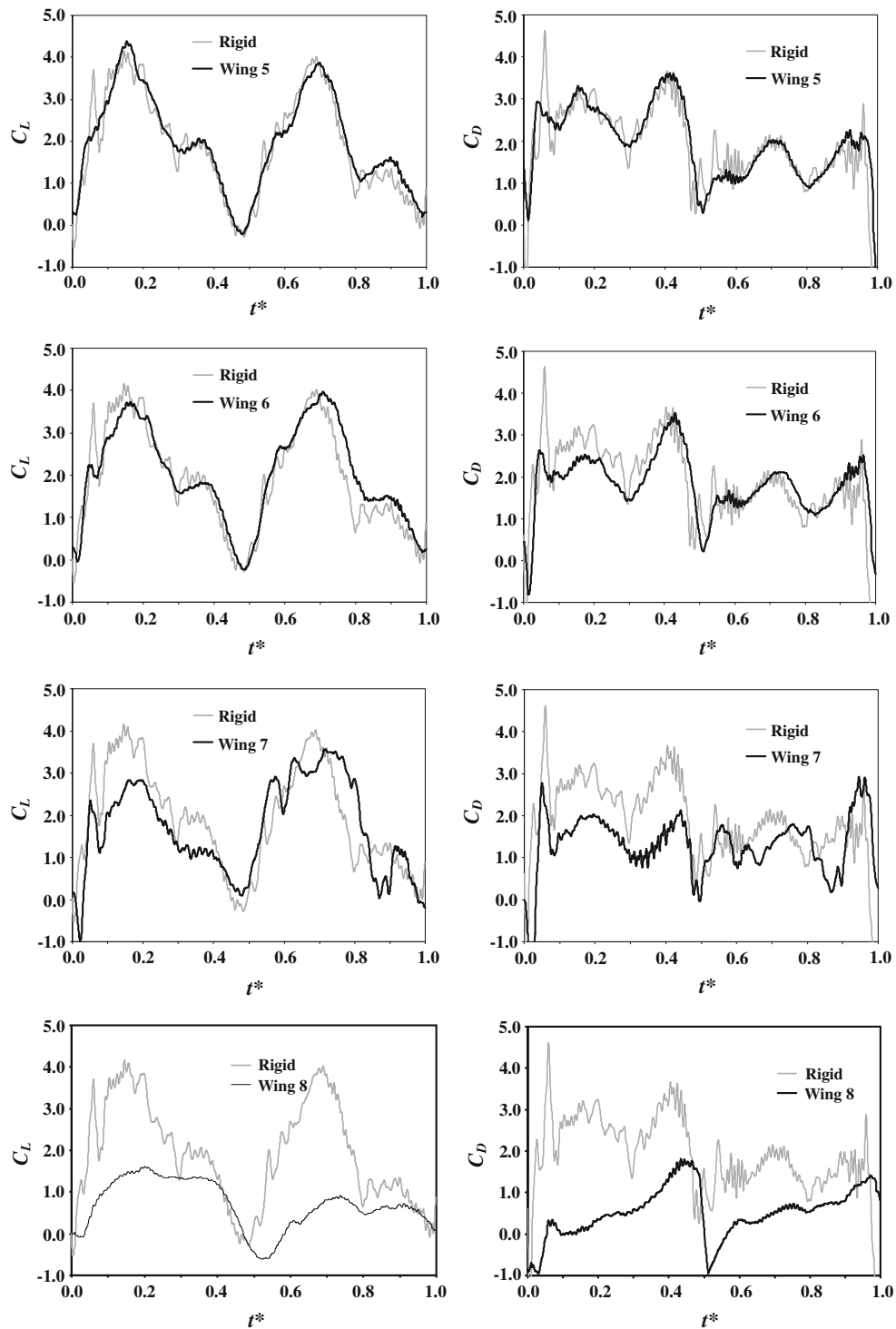


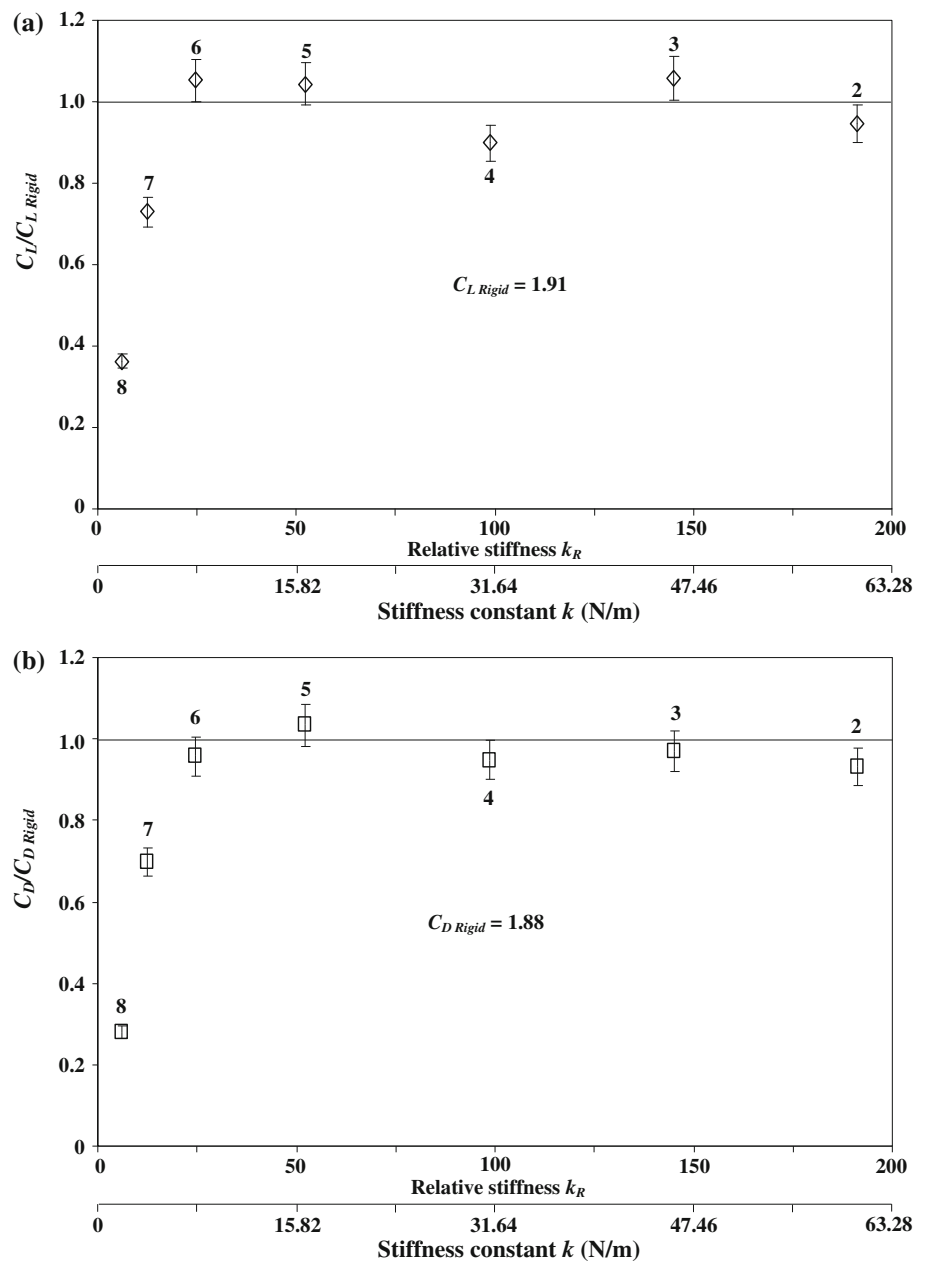
**Fig. 16** continued

Error bars of 5% are also indicated in the figure. It is obvious from Fig. 17 that the flexibility in Wing 2 to Wing 6 does not have significant effect on the mean aerodynamic force characteristics compared to the rigid wing, while Wing 7 and Wing 8 show considerable deterioration in both

the lift and the drag behavior. This finding is significant as it means that flexible wing, which is often light weight, can be used in MAV applications without significantly affecting its aerodynamic performance. But excessive flexibility can lead to deterioration in force generation.



**Fig. 17** Force coefficients of flexible wings normalized with the respective values of the rigid wing undergoing hawkmoth motion. **a** Lift coefficient. **b** Drag coefficient



### 3.2 Simple harmonic motion (SHM)

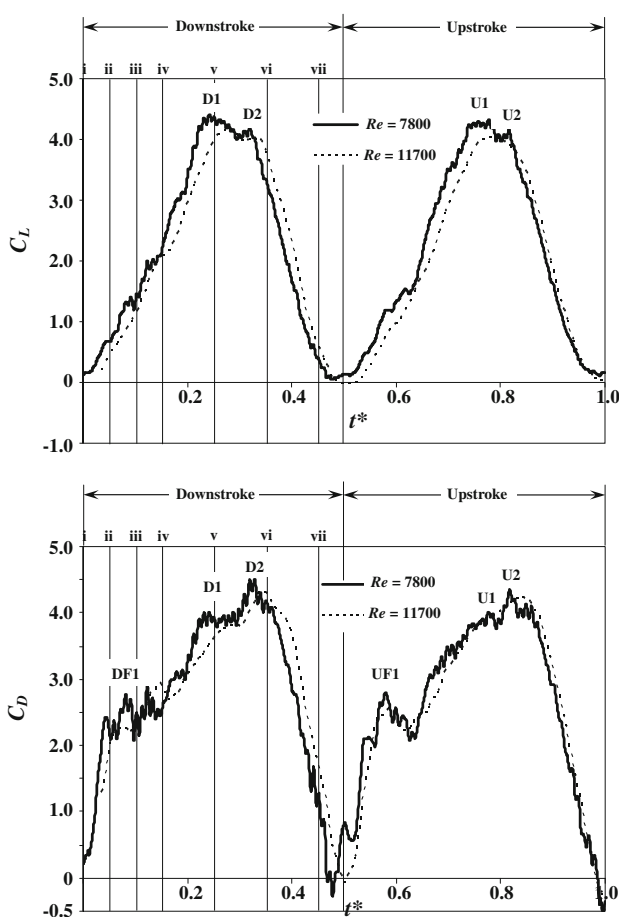
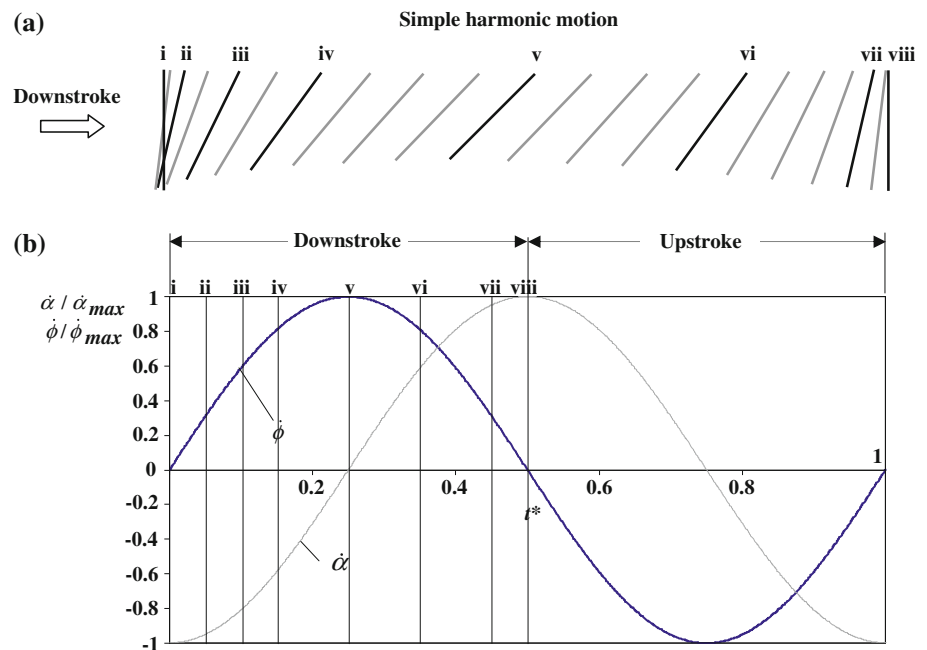
#### 3.2.1 Rigid wing

Figure 18 schematically shows the motion and the trajectory of a rigid wing performing SHM, and Fig. 19 shows the temporal force coefficients of a rigid hawkmoth-like wing subjected to SHM for the Reynolds numbers of 7,800 and 11,700. The corresponding vortex generation and shedding process are shown in the authors’ interpretation in Fig. 20. For ease of discussion, we will first describe the force characteristics, follows by a detailed discussion of the

vortex structures, and how these structures are linked to the measured forces.

Figure 19 clearly shows that the range of Reynolds number investigated here has insignificant effect on the force generation. In this regard, the numerical results of Aono and Liu (2008) for  $Re = 134$  (fruitfly flapping motion) and  $Re = 6,300$  (hawkmoth flapping motion) show that although the lower Reynolds number case has a lower spanwise or axial flow along the core of LEV, both cases exhibit similar topological vortex structures. Since SHM flapping motion is symmetrical in nature, it is not unexpected to see the results in Fig. 19 displaying comparable

**Fig. 18** Simple harmonic motion (SHM). **a** Schematic drawing of wing positions and instantaneous angles of attack,  $\alpha$ . **b** Instantaneous sweeping ( $\dot{\phi}$ ) and elevating ( $\dot{\theta}$ ) velocities for one flapping cycle



**Fig. 19** Time histories of lift and drag coefficients of Wing 1 (i.e., rigid wing) executing a simple harmonic motion for  $Re = 7,800$  and  $Re = 11,700$

drag forces during the upstroke and the downstroke. Detailed analysis shows that the mean  $C_D$  for the downstroke and the upstroke is 2.82 and 2.66, respectively, which effectively indicates a near zero mean horizontal force vectors over one complete cycle. This is consistent with the zero overall thrust condition of a hovering flight.

The sinusoidal nature of a simple harmonic wing motion is reflected in a sinusoidal-like  $C_L$  distribution with maximum values occurring at roughly the midpoint of the downstroke (D1) or the upstroke (U1), followed by a noticeable second peaks (D2 and U2). The first peak in the downstroke (D1) coincides with the maximum sweeping velocity at  $t^* = 0.250$ , and during this period (see Fig. 20i–vi), the generation of LEV plays an important role in the lift production. As the wing starts to slow down after reaching the maximum velocity around  $t^* = 0.250$ , the lift also decreases accordingly, but the simultaneous pitching up of the wing seems to dominate over the initial slowing down of the wing, thus causing a second peak D2. Since the sequence of events that occur during the upstroke is similar to that of the downstroke, the same reasoning can be applied to the existence of the two peaks (U1 and U2) during the upstroke. As for  $C_D$  distribution in Fig. 19b, the trend is distinctively different from the  $C_L$  distribution. Generally, there is a steep increase in the  $C_D$  value near the start of each stroke. In the case of the downstroke, this occurs around  $t^* = 0.000$  to slightly after  $t^* = 0.050$ . The steep increase in drag at the beginning of the stroke is not unexpected since the wing is accelerating at an angle of attack of  $90^\circ$ , but the more gentle increase that occurs soon

after can be attributed to a higher sweeping velocity and the generation of LEV. The drag continues to increase until it reaches a local peak value (D1) when the maximum sweeping velocity is reached at  $t^* \approx 0.250$ . Despite the wing slowing down after reaching a maximum sweeping velocity, the drag keeps increasing to reach the second peak as indicated by D2. Like the lift distribution discussed earlier, this peak is due to the dominant effect of the pitching up motion of the wing over the wing slowing down. Since the flapping motion is symmetrical, the drag coefficient distribution during the upstroke is generally similar to that of the downstroke, although the peak UF1 is more prominent than DF1, and U1 and U2 are less distinctive than D1 and D2. In an attempt to identify the cause of these differences, we examine closely the video replay of the captured images, which unfortunately do not reveal significant differences in the vortex structures between the downstroke and the upstroke.

Our flow visualization shows that, unlike the hawkmoth motion, the flow development of SHM consists of only two stages, i.e., the “initial stage” and the “vortex formation stage”. The “finishing state”, in which the LEV starts to shed from the leading edge, does not appear with SHM. The absence of the elevating motion in SHM when the wing is slowing down at the end of a stroke could be responsible for it. The “initial stage” covers from  $t^* = 0.000$  to 0.100. At this stage when  $t^* = 0.000$  (see Fig. 20i), the  $U_{LEV}$  formed in previous upstroke is still attached to the wing surface, but the replay of video recording appears to show that it is weak and diffused. This could be due to the fluid inertia pushing and compressing the LEV against the wing surface, thereby enhancing viscous diffusion when the wing stops momentarily before reversing its direction of motion. When the wing starts to accelerate during its downstroke motion (see Fig. 20ii, iii), the  $U_{LEV}$  is weakened further and eventually shed from the trailing edge. Meanwhile, a vortex loop is formed around the peripheral of the wing profile. The shedding of leading edge vortex generated in previous stroke from the trailing edge after the wing has reversed its direction to start a new stroke was also observed in the experiment of Poelma et al. (2006) involving a rigid fruitfly wing subjected to a simplified flapping motion. In the absence of elevating motion similar to the simple harmonic motion investigated in the present study, their wing accelerated quickly at the beginning of each stroke with a constant angle of attack and then rotated only prior to the end of the stroke. This caused the leading edge vortex to shed from the trailing edge of the wing, and then interact with the trailing edge vortex to form a vortex pair. Their finding is consistent with our observation of the formation of the vortex structure at the trailing edge as shown in Fig. 20iii, iv.

As part of the vortex loop at the trailing edge is shed to become  $D_{TEV}$  (see Fig. 20iv–vii), the flow enters the second “vortex formation stage”. Here, a distorted vortex loop is formed as the  $D_{RV}$  and  $D_{TV}$  trace the path of wing root and tip, while convecting with  $D_{TEV}$ . The  $D_{LEV}$  stays attached to the wing surface until the end of the downstroke, only to be weakened further when it compresses against the decelerating wing. Our video replay shows the presence of a rather strong axial flow when the

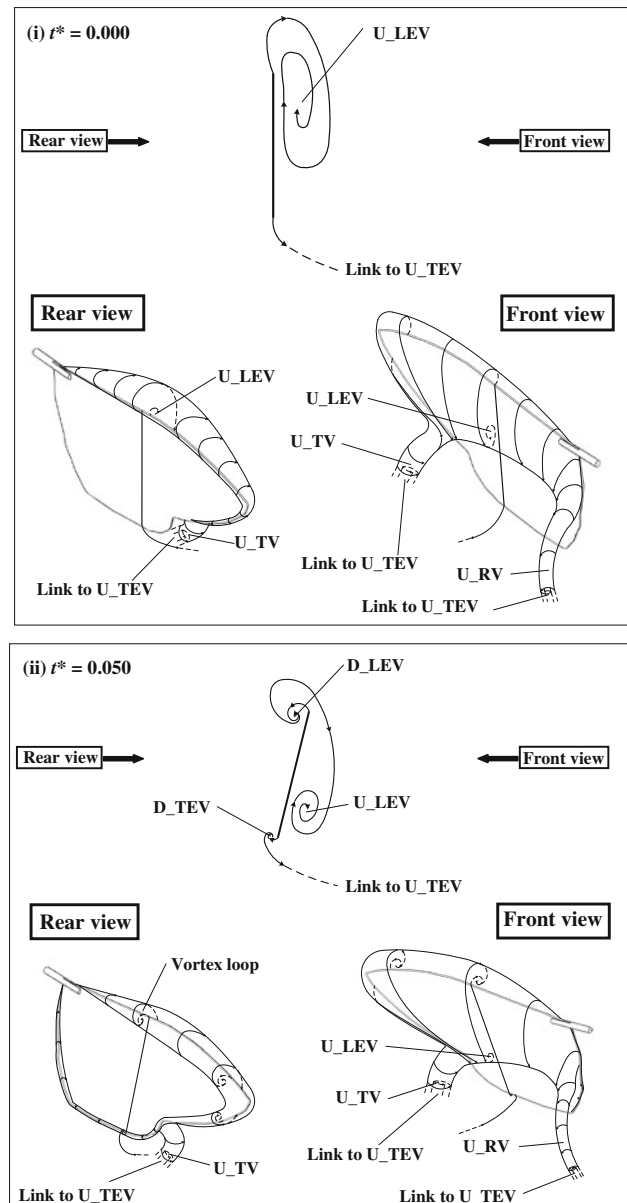


**Fig. 20** Sketches showing the authors’ interpretation of the flow development when a rigid wing is executing a simple harmonic motion. Each frame is selected to coincide with the salient features of the force measurements in Fig. 19. Note: the overall flow patterns for the upstroke are similar to those of the downstroke, and therefore not presented here

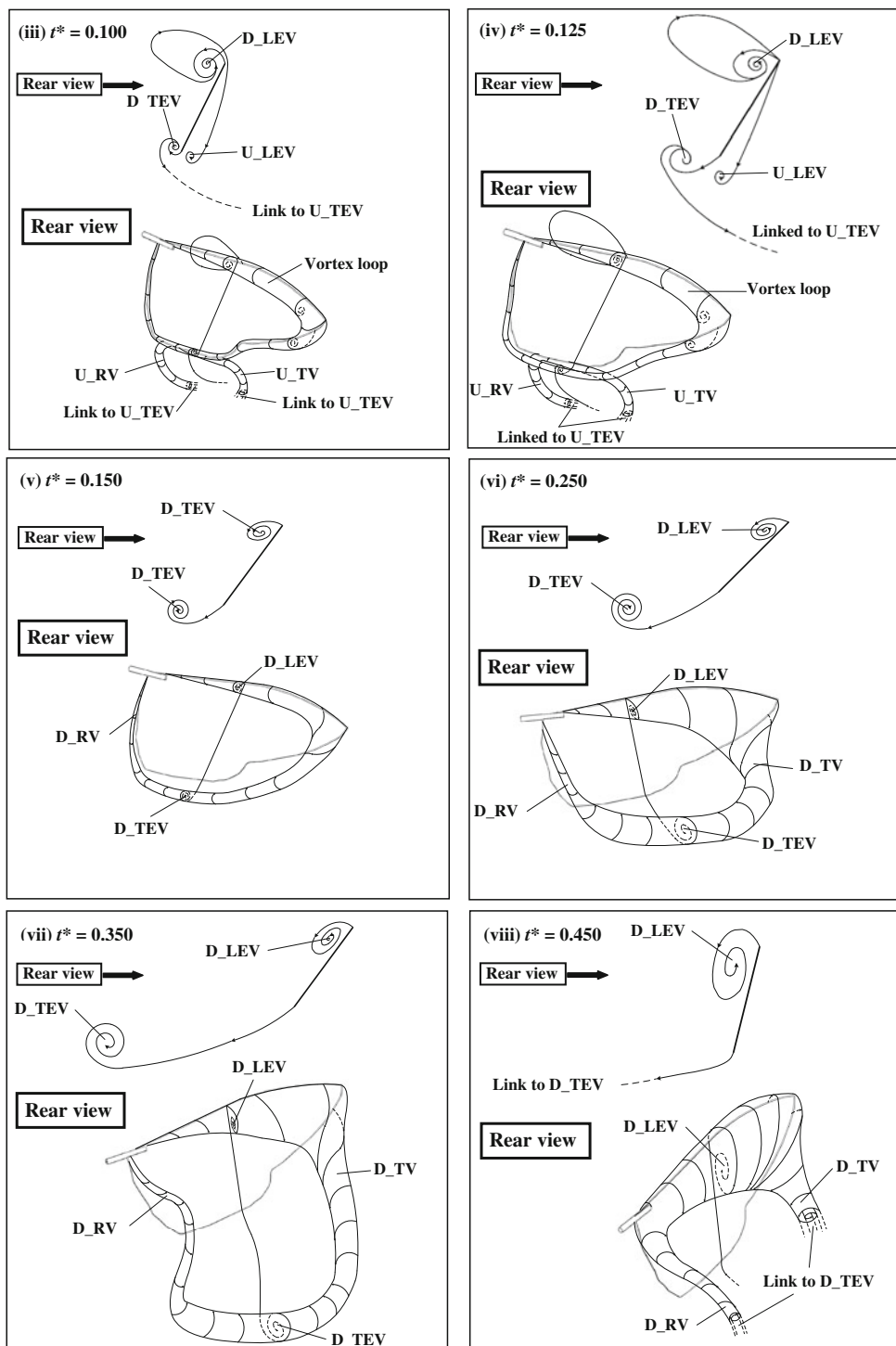


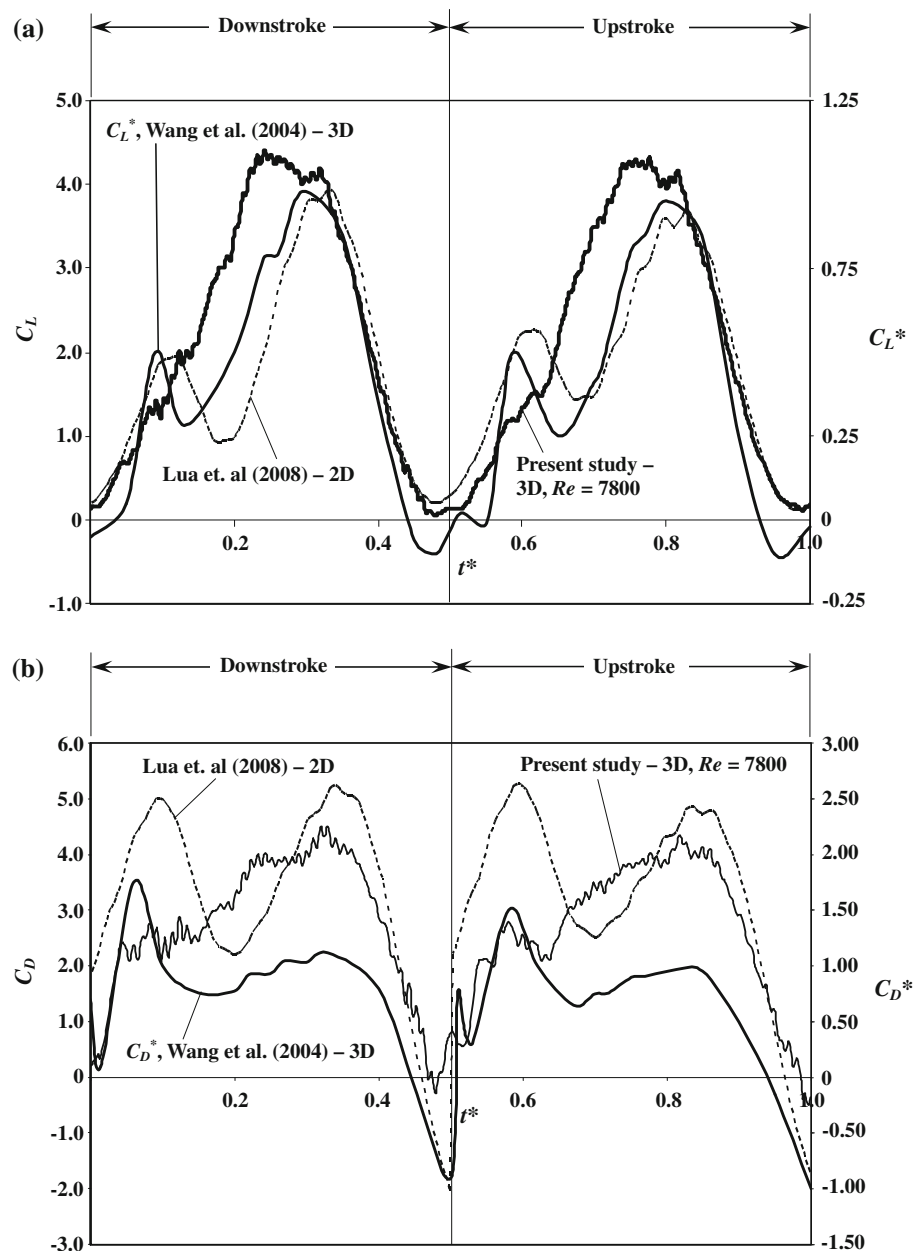
Fig. 20 continued

wing is sweeping through the middle of the stroke at high velocity.

The patterns of lift and drag coefficients shown in Fig. 19 are very different from the force characteristics of a 2-D simple harmonic flapping wing reported in Lua et al. (2008), and a 3-D simple harmonic flapping wing presented

in Wang et al. (2004). The data in Fig. 19 are re-plotted in Fig. 21 together with the results shown in Fig. 16 of Lua et al. (2008) (sharp edges bi-concave cross-sectional wing, Reynolds number based on root mean squared velocity equals to 1,326, stroke amplitude equals to three chord lengths,  $\beta = 45^\circ$ , lift and drag coefficients converted based

**Fig. 21** Comparison between the rigid wing executing simple harmonic motion with the publish data on the 2-D wing (Lua et al. 2008) and 3-D wing (Wang et al. 2004). **a** Lift coefficient ( $C_L$ ). **b** Drag coefficient ( $C_D$ )



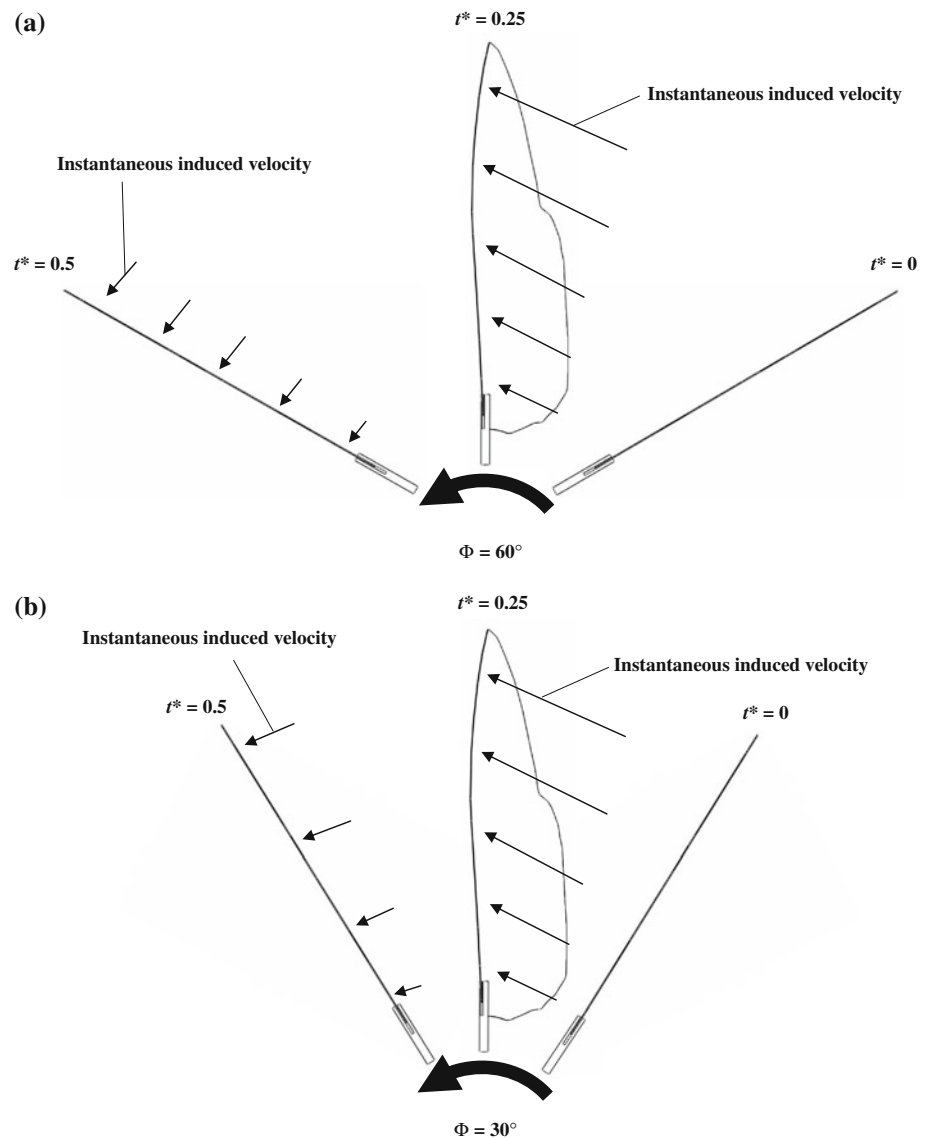
on the definitions of present paper) and the results shown in Fig. 3 of Wang et al. (2004) (Plexiglas *Drosophila* wing, Reynolds number based on maximum velocity equals to 75,  $\beta = 45^\circ$ , stroke amplitude =  $60^\circ$  (i.e.,  $\Phi = 30^\circ$ ),  $C_L^*$  and  $C_D^*$  are the lift and drag normalized by the corresponding maximum quasi-steady forces, the scales are shown at the right-hand side of Fig. 21a, b). Different scales are used in Fig. 21 for  $C_L$  and  $C_L^*$ ,  $C_D$  and  $C_D^*$ , as the purpose is to compare transient pattern only, not the magnitude.

The lift and drag distributions of both 2-D flapping wing and 3-D *Drosophila* wing show an apparent “dual-peak” pattern over a single stroke of flapping. The first peak is probably caused by the wing acceleration and the “induced

velocity” of the attached leading edge vortex formed in previous stroke. The second peak may be due to the new leading edge vortex formed in the current stroke and also the wing pitching up motion. The first peak in the transient  $C_L$  over one stroke of flapping is missing in the present experiment. Likewise, the first peak in the transient  $C_D$  is also missing (in downstroke) or greatly reduced (in upstroke). The reason may be due to the 3-D nature of the flow. In 2-D flow, all the vorticity sheds from the leading edge accumulates in the leading edge vortex, the strength of the leading edge vortex remains strong even when the wing slows down and stops. Thus, at the beginning of a 2-D stroke, the wing actually moves against the strong induced velocity of the leading edge vortex. In the present case of



**Fig. 22** Schematic drawings showing the induced flow conditions when **a**  $\phi = 120^\circ$  and **b**  $\phi = 60^\circ$



3-D flapping motion, the axial flow carries away the strong vorticity in the leading edge vortex when the wing is flapping with a high sweeping velocity. As demonstrated schematically in Fig. 22a,  $\Phi = 60^\circ$ , when the wing slows down and eventually stops, the leading edge vortex is much weaker than when it was at the middle of the stroke. Since the wing only encounters the induced velocity of the weaker leading edge vortex at the beginning of next stroke, the effect is too weak for the sensor to pick up.

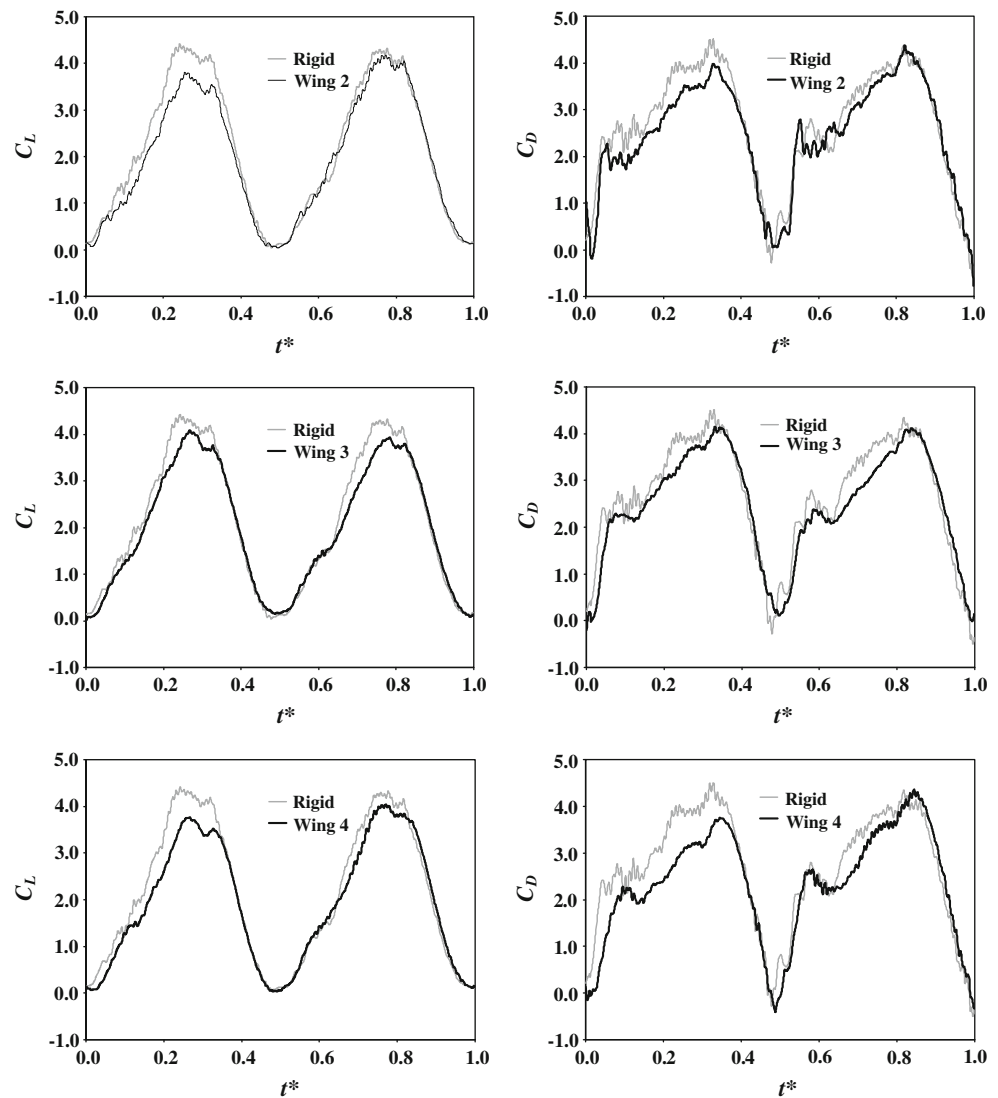
On the other hand, the high first peak in the transient forces of 3-D *Drosophila* wing may be caused by its small sweeping amplitude ( $\Phi = 30^\circ$ ). When the sweeping amplitude is small (see Fig. 22b,  $\Phi = 30^\circ$ ), the wing stops and reverses in the wake that induced at a high sweeping velocity, thus causing a very large peak in the forces. This postulation is supported by the advanced rotation results depicted in Fig. 5 of Wang et al. (2004). (although only

advanced rotation case was shown, the author claimed that the results are similar for symmetric rotation). When the stroke amplitude is increased from  $60^\circ$  to  $80^\circ$  and eventually to  $100^\circ$  (i.e.,  $\Phi = 30^\circ$ ,  $40^\circ$  and  $50^\circ$ ) with fixed flapping frequency, the magnitude of the first peak is reduced. It eventually vanished in the lift distribution and reduced to very small magnitude in drag distribution.

### 3.2.2 Flexible wing

In Fig. 23, the temporal lift and drag coefficients of the flexible wings (i.e., Wing 2 to Wing 8) are presented against the corresponding results of the rigid wing for the purpose of comparison. The figure clearly shows that Wing 2 to Wing 6 produce lower lift and drag distributions than the rigid wing. As the wing becomes more flexible (i.e., Wing 7 and Wing 8), its aerodynamic performance in terms

**Fig. 23** Comparison of the lift and drag coefficients of flexible Wing 2 to Wing 8 with a rigid wing (Wing 1) executing simple harmonic motion. *Left column:* lift coefficient ( $C_L$ ). *Right column:* drag coefficient ( $C_D$ )



of force generation deteriorates significantly. This behavior can be better observed in Fig. 24, where the mean lift and drag coefficients of the flexible wings relative to the rigid wing are presented with error bars of 5% and against both the relative stiffness and the stiffness constant. Like the hawkmoth flapping motion discussed earlier, if the wing stiffness constant falls below some critical value, there is a significant reduction in the aerodynamic force generation. But unlike the hawkmoth motion, Wing 2 to Wing 6 generates aerodynamic forces slightly below those of the rigid wing when executing a simple harmonic motion. Nevertheless, the results suggest that these flexible wings, when executing SHM, can generate flow field that is not significantly different from that of a rigid wing. As for the other two more flexible wings (Wing 7 and Wing 8), the severe bending of the wings have undoubtedly altered the vortex generation and shedding process significantly.

Although the above results show that wing flexibility below a certain critical value worsen aerodynamic performance due to bending and twisting, they also provide useful clue that wings with more axial stiffness (instead of homogeneous flexibility), while maintaining the chordwise flexibility would be a better choice for flapping wing vehicle, as this has an added advantage that aerodynamic force generation can be manipulated by adjusting the kinematic at its base to control wing twisting without compromising on its light weight.

### 3.2.3 Deflection angle

For completeness of this investigation, Fig. 25 presents the estimated wing deflection angle as a function of stiffness constant for all except the rigid wing (i.e., Wing 1), which has significantly less deflection. The tendency of higher

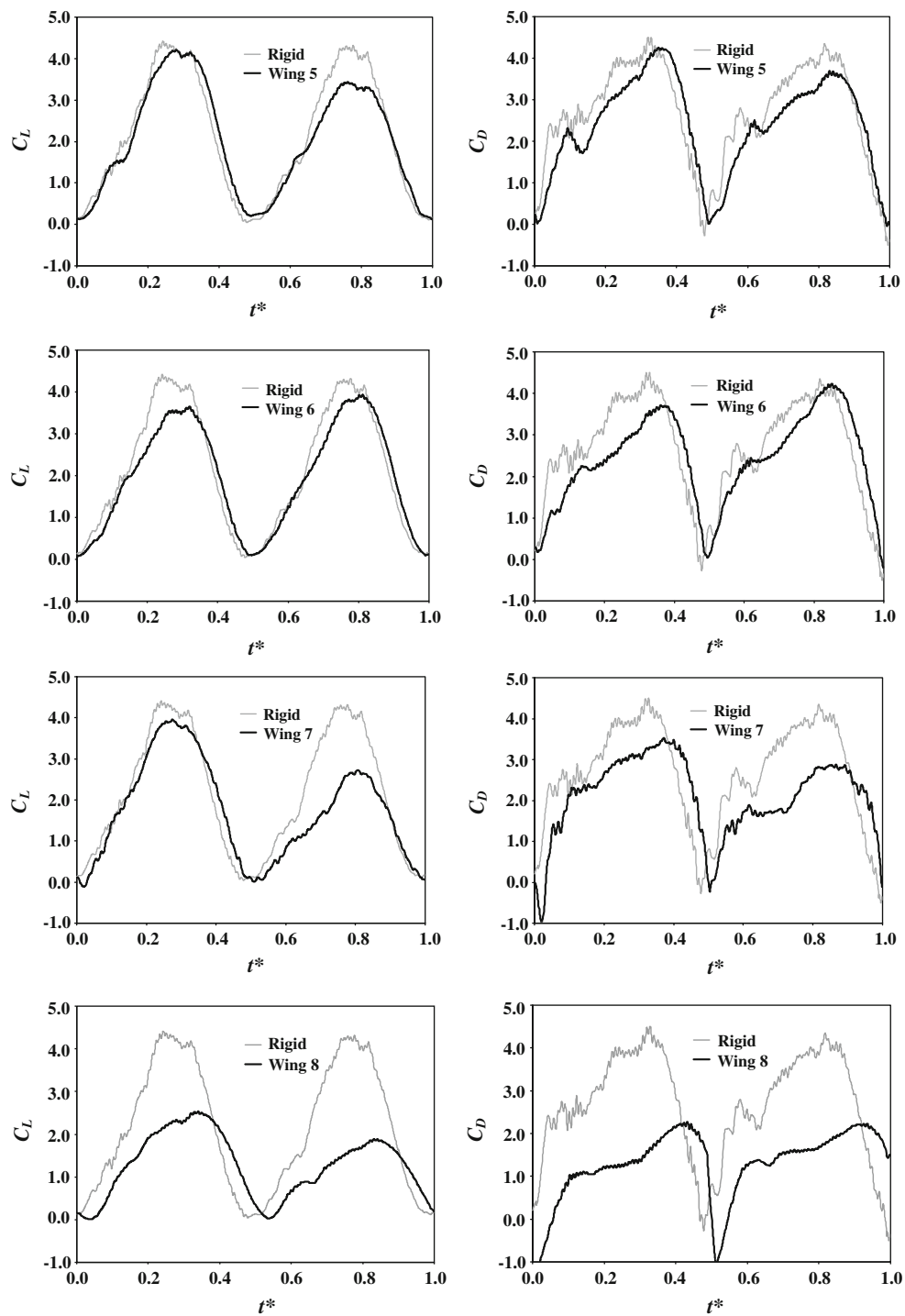


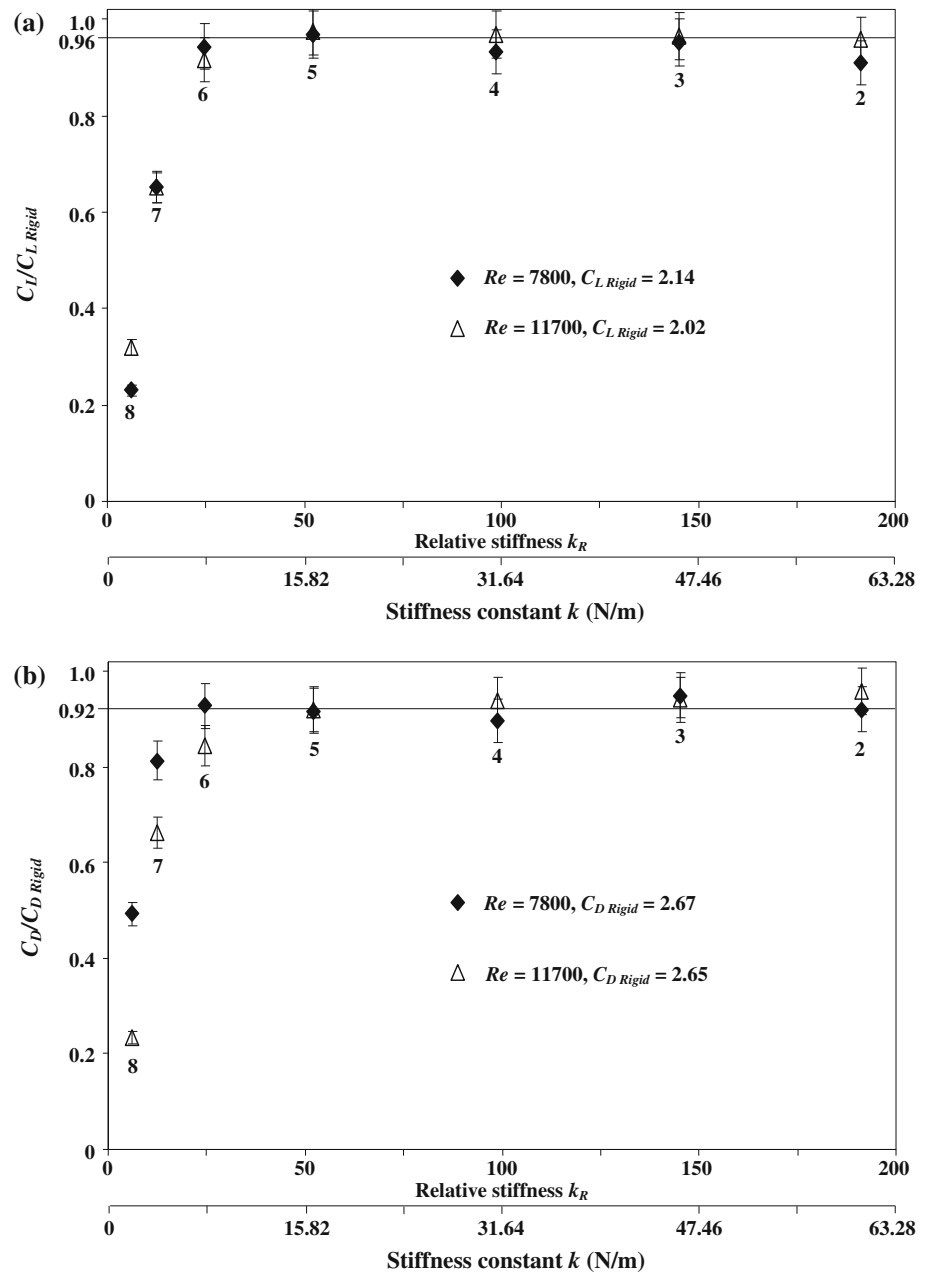
**Fig. 23** continued

stiffness constant causing lower deflection angle is not unexpected, although the exponential trend is interesting. It is also not unexpected that a lower Reynolds number leads to a lower deflection angle.

#### 4 Conclusions

The effects of wing flexibility on the generation of aerodynamic forces by a hawkmoth wing model executing

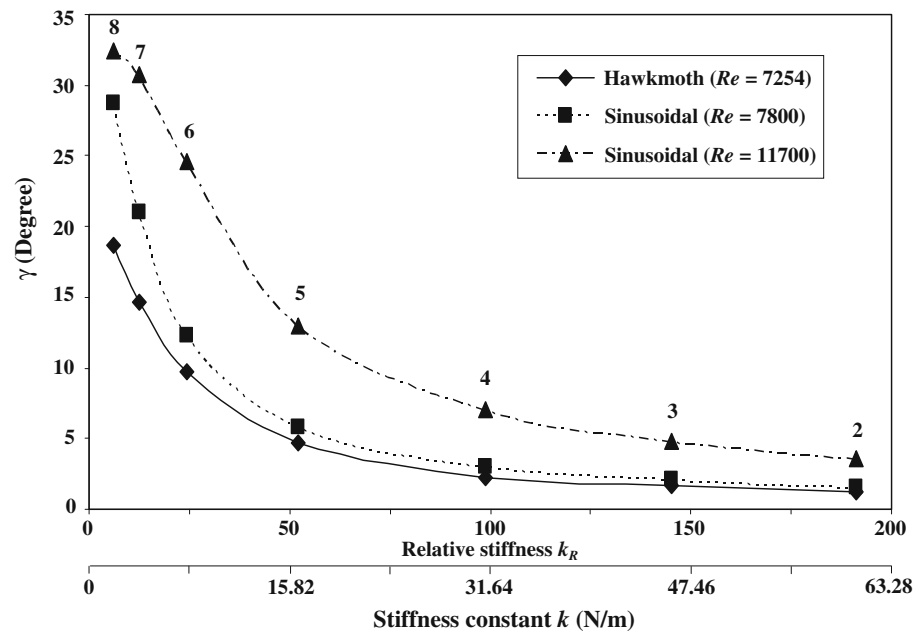
**Fig. 24** Force coefficients of flexible wings normalized with the respective values of the rigid wing undergoing simple harmonic motion. **a** Lift coefficient. **b** Drag coefficient



hovering hawkmoth flapping motion and a simple harmonic motion have been investigated. Hawkmoth motion was conducted at  $Re = 7,254$  and reduced frequency of 0.26, while simple harmonic flapping motion at  $Re = 7,800$  and 11,700, and reduced frequency of 0.25. The measured forces and the associated vortex structures for a rigid wing are used as the benchmark case for the flexible wings. Flow visualization results of the rigid wing show that a vortex loop is generated during each stroke of flapping motion, regardless of whether it is the hawkmoth motion or a simple harmonic motion. However, the strength of the vortex loop is kinematics dependent, which in turn affects force generation. On the other hand, the

remnant of the vortices generated in previous strokes does not have significant influence on the force generation. Our results further show that, provided wing stiffness constant does not fall below some “critical” value, flexible wing can generate lift and drag coefficients of comparable values to those of a rigid wing executing hawkmoth flapping motion, but slightly less than the rigid wing when undergoing simple harmonic motion. Below the “critical” stiffness constant, there is a drastic drop in the lift and drag coefficients as the wing becomes more susceptible to severe bending during flapping. This finding suggests that while flexible wing may have a practical advantage of being light weight (particularly in MAV application), too

**Fig. 25** Averaged deflection angle for wings undergoing Hawkmoth and simple harmonic motion



flexible a wing can cause deterioration in the aerodynamic performance. For the flow parameters considered here, our study also shows that Reynolds number ( $7,800 \leq Re \leq 11,700$ ) does not have significant influence on the force generation. Whilst the lift and drag coefficients computed by Aono and Liu (2008) for a hawkmoth wing undergoing hawkmoth flapping motion are broadly in agreement with our experimental results in terms of their overall trend, there are some noticeable differences in the details. The reason for the discrepancy remains unclear.

In closing, we reiterate that although hawkmoth wing model and flapping motion are used in the present study, they are not mimicking a real hawkmoth insect because the structural properties of the real wing are significantly more complex to model experimentally. The hawkmoth wing and kinematics are used only as a mean to an end, and at the same time to provide benchmark experimental database for numerical validation.

## References

- Aono H, Liu H (2008) A numerical study of hovering aerodynamics in flapping insect flight, Bio mechanisms of swimming and flying. Springer, Japan
- Aono H, Shyy W, Liu H (2009) Near wake vortex dynamics of a hovering hawkmoth. *Acta Mech Sin* 25(1):23–36
- Birch JM, Dickinson MH (2001) Spanwise flow and the attachment of leading-edge vortex on insect wings. *Nature* 412:729–732
- Combes SA, Daniel TL (2003a) Flexural stiffness in insect Wings I. Scaling and the influence of wing venation. *J Exp Biol* 206(17):2979–2987
- Combes SA, Daniel TL (2003b) Into thin air: contributions of aerodynamic and inertial-elastic forces to wing bending in the hawkmoth *Manduca Sexta*. *J Exp Biol* 206(17):2999–3006
- Deng X, Schenato L, Wu WC, Sastry SS (2006a) Flapping flight for biomimetic insects: part I-system modeling. *IEEE Trans Robot* 22(4):776–788
- Deng X, Schenato L, Sastry SS (2006b) Flapping flight for biomimetic insects: part II-flight control design. *IEEE Trans Robot* 22(4):789–803
- Dickinson MH, Gotz KG (1993) Unsteady aerodynamic performance on model wings at low Reynolds numbers. *J Exp Biol* 174:45–64
- Dickinson MH, Lehmann F, Sane SP (1999) Wing rotation and the aerodynamic basis of insect flight. *Science* 284(5422):1954–1960
- Ellington CP (1984) The aerodynamics of hovering insect flight. II. Morphological parameters. *Philos Trans R Soc Lond B* 305(1122):17–40
- Ellington CP (1999) The novel aerodynamics of insect flight: applications to micro-air vehicles. *J Exp Biol* 202(23):3439–3448
- Ellington CP, Van Den Berg C, Willmott AP, Thomas ALR (1996) Leading-edge vortices in insect flight. *Nature* 384(6610):626–630
- Hamamoto M, Ohta Y, Hara K, Hisada T (2007) Application of fluid-structure interaction analysis to flapping flight of insects with deformable wings. *Adv Robot* 21(1–2):1–21
- Isaac KM, Colozza A, Rolwes J (2006) Force measurements on a flapping and pitching wing at low Reynolds numbers. *AIAA* 2006-0450
- Lehmann FO (2004) Aerial locomotion in flies and robots: kinematic control and aerodynamics of oscillating wings. *Anthr Strut Dev* 33(3):331–345
- Lehmann FO, Sane SP, Dickinson M (2005) The aerodynamics of wing-wing interaction in flapping insect wings. *J Exp Biol* 208(16):3075–3092
- Lim TT, Teo CJ, Lua KB, Yeo KS (2009) On the prolong attachment of leading edge vortex on a flapping wing. *Mod Phys Lett B* 23:357–360
- Liu H, Ellington CP, Kawachi K, Van Den Berg C, Willmott AP (1998) A computational fluid dynamic study of hawkmoth hovering. *J Exp Biol* 201(4):461–477
- Lua KB, Lim TT, Yeo KS (2008) Aerodynamic forces and flow fields of a two-dimensional hovering wing. *Exp Fluids* 45(6):1047–1065

- Mountcastle AM, Daniel TL (2009) Aerodynamic and functional consequences of wing compliance. *Exp Fluids* 46:873–882
- Mueller TJ (2001) Fixed and flapping wing aerodynamics for micro air vehicle applications. *AIAA Progress in Astronautics and Aeronautics*, Vol. 195, the American Institute of Aeronautics and Astronautics
- Pederzani J, Haj-Hariri H (2006) A numerical method for the analysis of flexible bodies in unsteady viscous flows. *Intern J Numer Methods Eng* 68:1096–1112
- Platzer MF, Jones KD, Young J, Lai JCS (2008) Flapping-wing aerodynamics: progress and challenges. *AIAA J* 46(9):2136–2149
- Poelma C, Dickson WB, Dickinson MH (2006) Time-resolved reconstruction of the full velocity field around a dynamically-scaled flapping wing. *Exp Fluids* 41:213–225
- Sane SP, Dickinson MH (2001) The control of flight force by a flapping wing: lift and drag production. *J Exp Biol* 204(19):2607–2626
- Shyy W, Lian YS, Tang J, Viieru D, Liu H (2008) *Aerodynamics of low Reynolds number flyers*. Cambridge University Press, Cambridge Aerospace Series
- Smith MJC (1996) Simulating moth wing aerodynamics: towards the development of flapping-wing technology. *AIAA J* 34(7):1348–1355
- Srygley RB, Thomas ALR (2002) Unconventional lift-generating mechanisms in free-flying butterflies. *Nature* 420(6916):660–663
- Sun M, Tang J (2002) Unsteady aerodynamic force generation by a model fruit fly wing in flapping motion. *J Exp Biol* 205:55–70
- Usherwood JR, Ellington CP (2001) The aerodynamics of revolving wings I. Model hawkmoth wings. *J Exp Biol* 205(11):1547–1564
- Van den Berg C, Ellington CP (1997) The three dimensional leading-edge vortex of a “hovering” model hawkmoth. *Phil Trans B* 352(1351):329–340
- Wang ZJ, Birch JM, Dickinson MH (2004) Unsteady forces and flows in low Reynolds number hovering flight: two-dimensional computations vs robotic wing experiments. *J Exp Biol* 207(3):449–460
- Weis-Fogh T (1973) Quick estimates of flight fitness in hovering animals including novel mechanisms for lift production. *J Exp Biol* 59(1):169–230
- Willmott AP, Ellington CP (1997a) The mechanics of flight in the hawkmoth *Manduca sexta* I. Kinematics of hovering and forward flight. *J Exp Biol* 200(21):2705–2722
- Willmott AP, Ellington CP (1997b) The mechanics of flight in the hawkmoth *Manduca sexta* II. Aerodynamic consequences of kinematic and morphological variation. *J Exp Biol* 200(21):2723–2745
- Wootton RJ (1992) Functional morphology of insect wings. *Annu Rev Entomol* 37:113–140
- Wootton RJ, Evans KE, Herbert R, Smith CW (2000) The hind wing of the desert locust (*Schistocerca gregaria* Forskal). I. Functional morphology and mode of operation. *J Exp Biol* 203:2921–2931
- Wootton RJ, Herbert RC, Young PG, Evans KE (2003) Approaches to the structural modelling of insect wings. *Philos Trans R Soc Lond B* 358(1437):1577–1587
- Wu JH, Sun M (2004) Unsteady aerodynamic forces of a flapping wing. *J Exp Biol* 207(7):1137–1150
- Young J, Lai JCS, Germain C (2008) Simulation and parameter variation of flapping-wing motion based on dragonfly hovering. *AIAA J* 46(4):918–924
- Young J, Walker SM, Bomphrey RJ, Taylor GK, Thomas ALR (2009) Details of insect wing design and deformation enhance aerodynamic function and flight efficiency. *Science* 325:1549–1552
- Zheng L, Wang X, Khan A, Vallance RR, Mittal RA (2009) Combined experimental-numerical study of the role of wing flexibility in insect flight. *AIAA* 2009-382